Schildgen, T., van der Beek, P. A., D'Arcy, M.,
Roda-Boluda, D. C., Orr, E., Wittmann, H. (2022):
Quantifying drainage-divide migration from
orographic rainfall over geologic timescales:
Sierra de Aconquija, southern Central Andes. -
Earth and Planetary Science Letters, 579, 117345.

https://doi.org/10.1016/j.epsl.2021.117345

Quantifying drainage-divide migration from orographic rainfall over geologic timescales: Sierra de Aconquija, southern Central Andes

Taylor F. Schildgen[a,b*], Peter A. van der Beek[b], Mitch D'Arcy[c], Duna Roda-Boluda[d], Elizabeth N. Orr[e], Hella Wittmann[a]

a. GFZ German Research Centre for Geosciences, Telegrafenberg, 14473 Potsdam, Germany

b. Institute for Geosciences, University of Potsdam, Karl-Liebknecht-Str. 24-25, 14476 Potsdam, Germany

c. Department of Earth, Ocean and Atmospheric Sciences, University of British Columbia, 2020-2207 Main Mall, Vancouver, British Columbia, V6T 1Z4, Canada

d. Department of Earth Sciences, Vrije Universiteit Amsterdam, De Boelelaan 1105, 1081 HV Amsterdam, Netherlands

e. School of Geographical Sciences, University of Bristol, University Road, Bristol BS8 1SS, United Kingdom

** Corresponding author, tschild@gfz-potsdam.de*

Abstract

Drainage-divide migration, controlled by rock-uplift and rainfall patterns, may play a major role in the geomorphic evolution of mountain ranges. However, divide-migration rates over geologic timescales have only been estimated by theoretical studies and remain empirically poorly constrained. Geomorphological evidence suggests that the Sierra de Aconquija, on the eastern side of the southern Central Andes, northwest Argentina, is undergoing active westward drainage-divide migration. The mountain range has been subjected to steep rock trajectories and pronounced orographic rainfall for the last several million years, presenting an ideal setting for using low-temperature thermochronometric data to explore its topographic evolution. We perform three-dimensional thermal-kinematic modeling of previously published thermochronometric data spanning the windward and leeward sides of the range to explore the most likely structural and topographic evolution of the range. We find that the data can be explained by scenarios involving drainage-divide migration alone, or by scenarios that also involve changes in the structures that have accommodated deformation through time. By combining new ^{10}Be-derived catchment-average denudation rates with geomorphic constraints on probable fault activity, we conclude that the evolution of the range was likely dominated by west-vergent faulting on a high-angle reverse fault underlying the range, together with westward drainage-divide migration at a rate of several km per million years. Our findings place new constraints on the magnitudes and rates of drainage-divide migration in real landscapes, quantify the effects of orographic rainfall and erosion on the topographic evolution of a mountain range, and highlight the importance of considering drainage-divide migration when interpreting thermochronometer age patterns.

Keywords: drainage-divide migration, landscape evolution, orographic rainfall, thermochronology, cosmogenic nuclides, Central Andes

1. Introduction

Orographic precipitation has long been predicted to play an important role in the evolution of mountain belts (Gilbert, 1877; Penck, 1924). Proposed climate-tectonic feedbacks rely on the idea that enhanced precipitation and associated faster erosion can affect deformation by modifying both the stress and temperature fields within an orogen (Dahlen and Suppe, 1988; Beaumont et al., 1992). In orogens where rocks are exhumed at a low angle, lateral rock advection can counteract asymmetric erosion rates associated with orographic rainfall, and topographic asymmetry is predominantly controlled by tectonics (Willett, 1999; He et al., 2021). Conversely, in tectonically inactive regions or mountain ranges dominated by steep rock trajectories, asymmetric erosion should leave a clear topographic imprint: lowering of slopes on the wetter, more rapidly eroding side of the range and steepening of slopes on the drier, more slowly eroding side would lead to drainage-divide migration toward the dry side of the range (Bonnet, 2009). Although it has remained difficult to document clear cases of orogen-scale climate-tectonic feedbacks (Whipple, 2009), ample evidence has emerged for drainage-divide migration. Several studies have estimated rates of divide migration over recent to millennial timescales (Struth et al., 2017; Dahlquist et al., 2018; Hu et al., 2021) or have reconstructed past drainage-divide positions that differ substantially from today based on thermochronometric data (Ehlers et al., 2006; Simon-Labric et al., 2014), geomorphic constraints (Oskin and Burbank, 2005; Prince et al., 2011; Schwanghart and Scherler, 2020), or sediment provenance (Frisch et al., 1998; Mark et al., 2016). When sustained on million-year timescales, lateral migration of topography in response to orographic rainfall patterns will impact rock-cooling histories and ensuing thermochronometric ages, because on the dry side, slower erosion suppresses exhumation, whereas on the wet side, faster erosion enhances exhumation. Two modeling studies have illustrated how thermochronometric data from both sides of a mountain range could be used to reconstruct lateral migration rates of topography (Stüwe and Hintermüller, 2000; Olen et al., 2012). However, to our knowledge, this approach has not yet been applied to field data, and despite the apparent commonality of the process, little work has been done to quantify rates of drainage-divide migration over geologic timescales.

Within the Central Andes of northwest Argentina, orographic rainfall focused on the eastern flanks of the mountain ranges (Fig. 1) is associated with high millennial-scale denudation rates derived from in situ ^{10}Be concentrations in river sand (Bookhagen and Strecker, 2012). This link appears to have persisted over at least the last ca. 6 million years, based on combined reconstructions of paleotopography and paleodenudation rates from the Humahuaca Basin (Pingel et al., 2019; Fig. 1). The Central Andes in northwest Argentina constitute an archetypal broken foreland, characterized by uplifted basement blocks adjacent to intermontane basins (Strecker et al., 2011). The persistent link between orographic rainfall and rapid erosion, together with the structural evidence for steep bounding faults along the uplifted basement blocks, creates ideal conditions to test how climate has affected landscape evolution over the last several million years in the region.

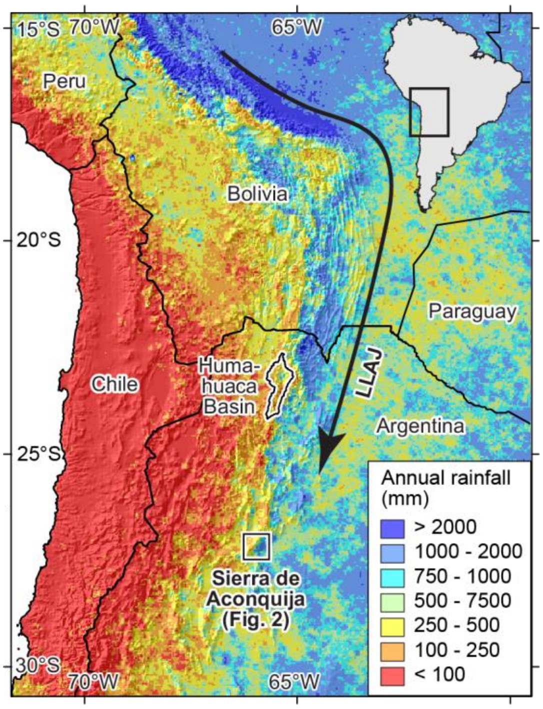

Figure 1. Location of the Sierra de Aconquija within the Central Andes. Colors show annual rainfall based on TRMM2B31 data (Bookhagen and Strecker, 2008) plotted over shaded relief. Throughout the Central Andes, the eastern flanks of individual ranges tend to receive the highest rainfall, which is partly related to southward moisture transport by the low-level Andean jet (LLAJ).

Several aspects of the Sierra de Aconquija, on the eastern margin of the southern Central Andes (Fig. 1), highlight the possibility that it has experienced sustained drainage-divide migration. Orographic rainfall along the lower, densely vegetated eastern flanks of the range increases to a peak of ca. 2000 mm/yr at elevations of 2000 m, then decreases to ca. 300 mm/yr at the range crest, and further drops to less than 250 mm/yr within the Santa María Basin to the west (Bookhagen and Strecker, 2008; Fig. 2). This pattern of orographic rainfall has not changed substantially during the last few glacial advances (ca. 40 ka, 22 ka, and 12-13 ka based on dated moraines; D'Arcy et al., 2019): the two most recent advances have been associated with minor decreases in temperature (of 1 to 4°C) and increases in precipitation (5-27%) relative to today (Mey et al., 2020). This strong and persistent gradient in rainfall could be responsible for the morphologic similarities Bonnet (2009) recognized between the Sierra de Aconquija and his physical experiments of divide migration, with drainage basins on the dry (west) side of the range showing evidence of recent shortening and splitting. Channel morphology on the wet (east) side of the range also shows a pattern consistent with orographic rainfall, with reduced steepness values of tributary channels along the lower, wetter slopes compared to tributaries from the upper, drier flanks (Fig. 2d). Moreover, steepness values along the trunk streams increase smoothly upstream despite uniform lithology, as expected if greater rainfall rates and higher discharge lead to increased downstream erodibility (D'Arcy and Whittaker, 2014; Han et al., 2015). Finally, published thermochronometric ages from the wet side of the range are consistently younger than those on the dry side at similar elevations (Sobel and Strecker, 2003; Löbens et al., 2013; Figs. 2, 3), mimicking the age-elevation patterns predicted by Stüwe and Hintermüller (2000) and Olen et al. (2012) for laterally shifting topography.

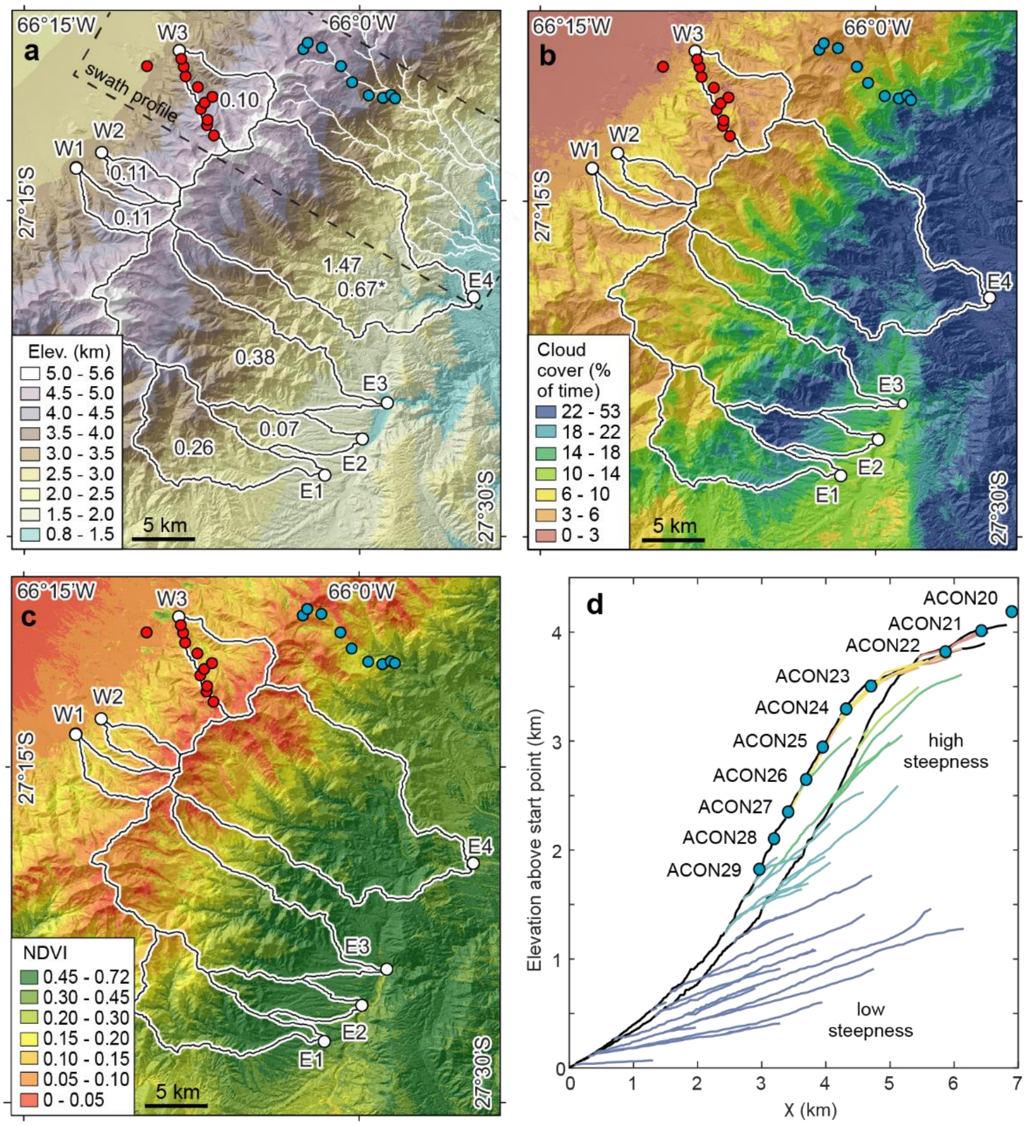

Figure 2. Study area at Sierra de Aconquija with sample locations. White circles show locations of river-sand samples for ^{10}Be analysis; red and blue circles show locations of thermochronometer samples from dry (Sobel and Strecker, 2003) and wet (Löbens et al., 2013) flanks of the range, respectively. a) Color-coded elevation over shaded relief, from TanDEM-X digital elevation data. Numbers inside catchments show catchment-average denudation rates (mm/yr) derived from ^{10}Be analysis. Rate with asterisk is recalculated from data presented in Bookhagen and Strecker (2012); all other rates are from this study. Dashed line shows extent of swath profile in Fig. 3a. b) Color-coded percentage of time with cloud cover, based on ca. 21 years of Landsat 7 data (average of 433 images), plotted over shaded relief. c) Color-coded normalized difference vegetation index (NDVI), derived from ca. 21 years of Landsat 7 data (average of 21 yearly-averaged images), plotted over shaded relief. Panels (b) and (c) provide a high-resolution proxy for rainfall. d) Chi-plot of all channels with a minimum drainage area of 1 km^2 within the catchment that includes thermochronometer samples from the east side of the range (white channels in panel a), using a reference concavity index of 0.45. The slope of a channel on a chi plot scales with the channel steepness value; note the lack of a change in slope along the trunk stream between samples ACON28 and ACON29. Tributaries are colored according to mean cloud cover, as in panel (b); trunk streams are black. Starting point is off the map, and was chosen to include the other major tributary in the catchment. Note that tributary channels at lower elevation have lower slopes (hence lower steepness values) compared to tributary channels at higher elevation. Chi plots of the other catchments on the wet side show similar patterns.

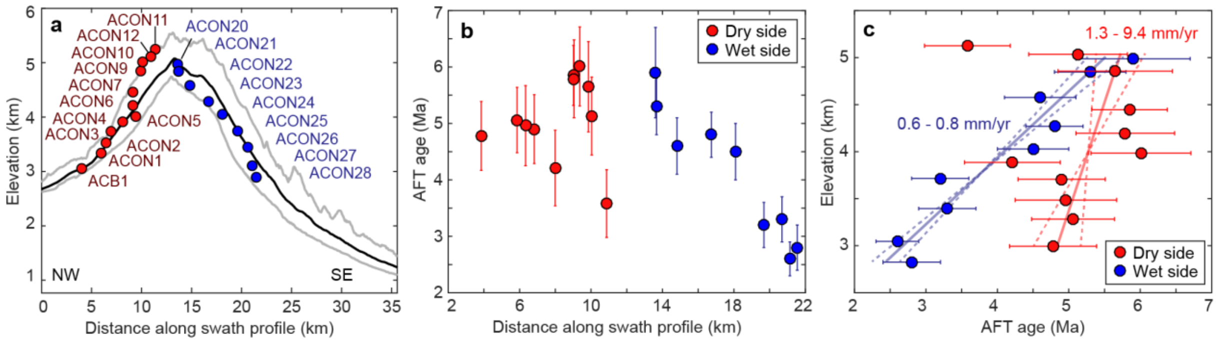

Figure 3. Thermochronometric data from Sierra de Aconquija. Samples are from Sobel and Strecker (2003) on the western (dry) side in red and from Löbens et al. (2013) on the eastern (wet) side in blue. a) Sample locations plotted on 14-km wide swath profile. Black line shows mean elevation, gray lines show minimum and maximum elevations across the swath (location shown in Fig. 2a). b) Apatite fission-track (AFT) ages (with 1σ uncertainties) plotted against distance along swath profile. c) AFT ages (with 1σ uncertainties) plotted against elevation. Trend lines show best-fitting linear regression through wet and dry sides (dashed lines show 1σ uncertainties), with associated apparent exhumation rates. Highest sample on dry side showing anomalously young age was excluded when calculating the trend. This age was considered an outlier by the original study that reported it (see Sobel and Strecker, 2003, for discussion). Note that only 11 samples are plotted in panels (b) and (c) from the dry side, because sample ACON11 has a reported AHe age, but no reported AFT age.

Löbens et al. (2013) suggested that the pattern of thermochronometer ages from the Sierra de Aconquija could be explained by changes in the structures accommodating deformation over time, first dominantly east-vergent and later more symmetric, but the potential effects of topographic evolution on thermochronometer age patterns were not considered in their interpretations. Here, we use three-dimensional thermal-kinematic modeling to explore whether the pattern of thermochronometric ages across the Sierra de Aconquija can be used to distinguish among several potential landscape-evolution scenarios: drainage-divide migration (simulated through either a topographic shift or a topographic warp), structural evolution (i.e., a change in the deformation rates along faults and/or their position), or a combination of structural evolution and drainage-divide migration. Topographic metrics and new catchment-average ^{10}Be-derived denudation rates further allow us to evaluate whether any of these scenarios is likely to explain the evolution of this landscape.

2. Geologic, topographic, and climate history

The broken foreland of the Central Andes in northwest Argentina comprises uplifted basement blocks bounded by steep reverse faults that partly reactivated Cretaceous normal faults of the Salta Rift (Grier et al., 1991; Strecker et al., 2011 and references therein). The Sierra de Aconquija is composed of Precambrian to early Paleozoic metamorphic rocks and Paleozoic granites that are thrust above Neogene basin sediments on its NW and SE sides along high-angle reverse faults (Cristallini et al., 2004; Mortimer et al., 2007; Iaffa et al., 2013; Zapata et al., 2020; Fig. 4a). The shallow (i.e., within ca. 20 km of the surface) geometries of structures that cut through the basin sediments to the west and east of the Sierra de Aconquija are constrained by seismic reflection data, which show predominantly west-dipping faults to the east of the range and east-dipping faults to the west (Cristallini et al., 2004; Iaffa et al., 2013). In contrast, the geometries of faults directly beneath the range are poorly constrained. Cristallini et al. (2004) interpreted a few deep, prominent reflectors (Fig. 4a) to suggest that the main structure accommodating rock uplift of the Sierra de Aconquija is a west-vergent fault rooting in the middle to lower crust. Continued activity on that structure and associated faults is inferred from offset Quaternary alluvial fans at the toe of the western range flank (Strecker et al., 1989). Löbens et al. (2013) suggested a modification to this interpretation, based on the pattern of thermochronometer ages along the eastern flank of the range. Late-Miocene or younger apatite fission-track and (U-Th)/He ages characterize all the samples in the elevation transect except for one sample at the base (ACON29; Fig. 2d), which yielded Cretaceous-Paleogene ages. To explain the offset in ages, Löbens et al. (2013) inferred the existence of a major thrust with up to 9 km of west-side-up displacement mid-way up the eastern flank of the Sierra de Aconquija (Fault B1 in Fig. 4a). They suggested initial activity along that fault since ca. 9 Ma, followed by activation of the fault bounding the west side of the range between ca. 6 and ca. 3 Ma, and finally faulting on the east flank stepping out toward the foreland (Fault B2 in Fig. 4a). We have drawn those proposed east-vergent structures as (dashed) back-thrusts in Fig. 4a, but their geometries are unconstrained.

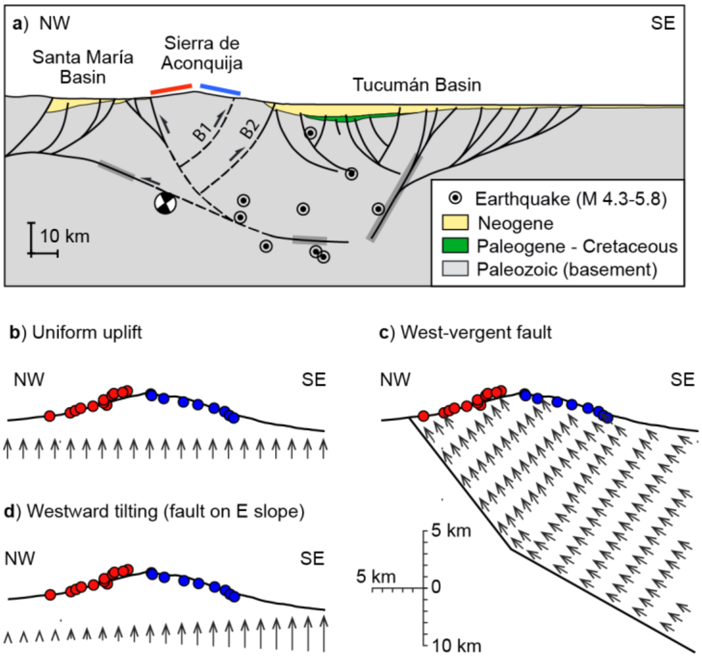

Figure 4. Structural cross-section of the Sierra de Aconquija and imposed deformation fields used in thermokinematic modeling. (a) Geologic cross-section based on seismic-line interpretations from Cristallini et al. (2004), with structures on SE flank of Aconquija (labeled B1 and B2) modified following Löbens et al. (2013). Geometry of structures is well constrained up to ca. 20 km depth beneath the Santa María and Tucumán basins. Geometry of deeper structures is constrained by seismic data in regions of the dark gray boxes; dashed lines indicate inferred geometry. Red and blue lines above topography show the spatial distribution of cooling ages reported by Sobel and Strecker (2003) and Löbens et al. (2013). Instrumental earthquakes (from USGS National Earthquake Information Center) within 100-km wide swath around the profile are projected into the profile; a single available focal mechanism is also shown (horizontal projection). (b) – (d) Illustrations of main classes of structural deformation imposed in thermal-kinematic modelling. Arrows indicate motion vectors of rock particles. Red and blue circles show locations of thermochronometer samples on the dry (red) and wet (blue) sides of the range, plotted on top of the mean elevation of the topographic swath profile shown in Fig. 3, limited to the spatial extent of the Pecube models. For simulations that include only drainage-divide migration, i.e., topographic shift or topographic warp, we assume a uniform vertical rock-uplift field (b). Motion on the west-vergent fault is simulated as in (c). Motion on the east-vergent back-thrusts is simulated through tilting (differential uplift), as in (d). Note that the vertical scale of the fault in (c) is reduced by a factor 2; i.e. in reality the fault is twice steeper than shown and soles out at 50 km depth.

Sedimentary records from the Santa María Basin, which borders the Sierra de Aconquija to the west (Fig. 4a), reflect substantial changes in climate and ecosystems over the last several million years, which appear to be closely linked to changes in topography. Carbon-isotope data reveal an increase in C_3 plant assemblages and inferred wetter conditions between ca. 5 and 3 Ma, which was interpreted to result from orographic rainfall triggered by uplift of the Sierra de Quilmes on the western side of the basin (Kleinert and Strecker, 2001). This interpretation is supported by the ca. 6 Ma onset of exhumation of the Sierra de Quilmes recorded by apatite fission-track ages (Mortimer et al., 2007). A shift to more C_4 plants between ca. 3.0 and 2.5 Ma was suggested to result from the Sierra de Aconquija having reached sufficient elevations to block incoming rainfall (Kleinert and Strecker, 2001). Similar scenarios of surface uplift of ranges controlling precipitation patterns have been derived from stable-isotope studies in several Central Andean sedimentary basins to the north (Pingel et al., 2014, 2016, 2020; Rohrmann et al., 2016).

Sedimentological and thermochronometric evidence also points to initial surface uplift of the Sierra de Aconquija by the early Pliocene. The first basement-derived conglomerates appeared in the Santa María basin within the ca. 5.0 to 3.4 Ma upper Andalhuala Formation, and those conglomerates dominate deposition in the ca. 3.4 to 3.0 Ma Corral Quemado Formation (Strecker et al., 1989; Bossi et al., 2001). Exhumation of the range likely started earlier, by ca. 6 Ma, based on time-temperature histories derived from apatite fission-track-length modeling (Sobel and Strecker, 2003). The time lag between the onset of cooling and the deposition of basement-derived conglomerates is likely a consequence of initial exhumation of the range being associated with the removal of ca. 1 km of sedimentary cover that had previously buried and reheated the basement rocks during the late Miocene (Sobel and Strecker, 2003).

3. Methods

3.1. Thermal-kinematic modeling of thermochronometric data

Drainage-divide migration can lead to differences in thermochronometer age-elevation relationships on either side of a range if the relevant closure isotherm is non-planar, i.e., at least partly mimics topography (Stüwe and Hintermüller, 2000). For example, in a setting with a topographic wavelength of 20 km and relief of 2 km, exhumation rates of at least 1 mm/yr are required for substantial deflection of the 100°C isotherm. Under these conditions, for a thermochronometer with a 100°C closure temperature, drainage-divide migration of at least ca. 2 mm/yr will produce detectable differences in cooling ages across the range (Stüwe and Hintermüller, 2000). However, because differences in age-elevation relationships across a range can result from either differences in topographic evolution or differences in rock-uplift history, we explore both possibilities in our modeling approach.

We use three-dimensional thermal-kinematic modeling (Pecube version 3; Braun et al., 2012) to first explore how drainage-divide migration affects patterns of low-temperature thermochronometer ages for a model based on the modern topography of the Sierra de Aconquija. For those model runs, we used a series of synthetic digital elevation models (DEMs) to simulate the topographic evolution associated with drainage-divide migration. One set of synthetic DEMs, used to simulate *topographic shift*, consists of the modern topography that has been translated laterally in 1-km increments up to a total of 10 km (Fig. 5a). A second set of DEMs, used to simulate *topographic warp*, consists of warped versions of the modern topography, with a warping function that takes the form of a sine curve: maximum spatial shifting (up to 10 km) occurs along the modern drainage divide, with the amount of shifting decreasing to 0 at the northwestern and southeastern edges of the model (Fig. 5b). All simulations start with a synthetic, shifted/warped DEM, and finish with the modern topography. For this first set of simulations, we explore the total magnitude, rate, and timing of migration.

These simulations allow us to compare our results to broadly similar scenarios modeled by Stüwe and Hintermüller (2000) and Olen et al. (2012).

Following this exploration of the general impact of drainage-divide migration on thermochronometer-age patterns, we use a second set of simulations to explore which landscape-evolution scenarios are consistent with the thermochronologic ages and topographic evolution reported from the Sierra de Aconquija. All of these models start with flat topography at 6 Ma at an elevation of 500 m, equal to the estimated elevation of the foreland prior to surface uplift, followed by topographic growth. We consider several potential scenarios of subsequent landscape evolution: drainage-divide migration (through topographic shift or topographic warp), structural evolution, and structural evolution combined with topographic warp.

To define the parameter space explored in the second set of simulations, we consider the geologic constraints described in section 2 with regards to the onset of exhumation (ca. 6 Ma), the time at which surface uplift must have started (ca. 5 Ma), and the time at which a minimum of 2 km of elevation must have been reached (ca. 2 Ma). Additional details on how these constraints translate into the range of parameter values we tested are provided in the Supplementary Material.

In the models that involve no structural evolution, we impose vertical rock uplift that is allowed to vary temporally but not spatially, implicitly assuming that both the western and eastern range-bounding faults are similarly active throughout the modeled timespan (Fig. 4b). We also test whether it is possible to explain the thermochronometer-age patterns purely through structural evolution of the range, or some combination of structural evolution and drainage-divide migration. In these scenarios, we include motion along a model fault (Braun et al., 2012) that simulates the main west-vergent structure bounding the western side of the Sierra de Aconquija inferred by Cristallini et al. (2004) (Fig. 4c). In one scenario, fault motion is combined with a lateral gradient in rock-uplift (i.e., westward tilting, Fig. 4d), to approximate the deformation field within the region of interest that would result from motion along steeply dipping east-vergent structures bounding the east side of the range (Faults B1 and B2 in Fig. 4a). Details of the model setup and model parameter values are provided in Table S2. Three-dimensional renditions of the input topography from two model runs are shown as examples in Fig. S1. Details of all simulations are summarized in Tables S3 and S4.

Thermal-kinematic modeling results are assessed qualitatively through comparisons between predicted and observed apatite fission-track (AFT) and apatite (U-Th)/He (AHe) age-elevation patterns on both sides of the range (Figs. 2, 3; Sobel and Strecker, 2003; Löbens et al., 2013), as well as quantitatively through examination of misfit values, for which we use the reduced χ^2 statistic (Braun et al., 2012). We include AHe ages where they are available and internally consistent with the AFT ages (i.e., AHe ages that are younger than AFT ages). We also include two available zircon (U-Th)/He (ZHe) age constraints (Löbens et al., 2013) in our assessments of misfit (Table S1). We exclude the ages reported by Löbens et al. (2013) from sample ACON29, the lowermost sample collected from the eastern side of the range, which are anomalously old (i.e., AFT age of 118 Ma compared to ca. 2 to 7 Ma for the other samples in the transect), as we focus our modeling on the final exhumation phase of landscape evolution. Our aim is not to conduct an exhaustive search of the parameter space to find the single best-fitting scenario, but rather to explore whether any of the scenarios we consider can produce reasonable fits to the thermochronologic data.

3.2. Catchment-average denudation rates and topographic evolution

We measured the concentration of *in-situ* produced ^{10}Be in river sands obtained from active channel bars in catchments on both sides of the Sierra de Aconquija (Fig. 2) to constrain millennial-scale denudation rates. Details of sample preparation and analysis of ^{10}Be concentrations are provided in the Supplementary Material.

We use differences in denudation rates from either side of the Sierra de Aconquija to estimate divide-migration rates. Fig. 5c illustrates how the denudation rates on the dry side (D_d) and wet (D_w) sides of the range are related to (1) the vertical component of topographic shift, which leads to either local surface uplift (U_s) or surface drop ($-U_s$), and (2) the regional rock-uplift rate (U_r), or specifically the vertical component of rock uplift:

$$D_w = U_r - (-U_s) \tag{1}$$

$$D_d = U_r - U_s \tag{2}$$

In the simple case of topographic shift of a mountain with symmetric slopes:

$$U_s = V_{shift} \tan(\alpha) \tag{3}$$

where V_{shift} is the rate of topographic shift and α is the mean slope of the range. Because the difference between the denudation rates on the wet and dry sides of the range, ($D_w - D_d$), is equal to twice the surface-uplift rate (Eq. 1, 2), that difference in denudation rates can be used to estimate V_{shift}:

$$V_{shift} = \frac{{}^1\!/_2 (D_w - D_d)}{\tan(\alpha)} \tag{4}$$

To estimate the drainage-divide migration rate for a topographic-warp scenario, we start with the same arguments with regard to solving for surface uplift (U_s) or surface drop ($-U_s$). On the wet flank of a range that is experiencing topographic warping, the surface-drop rate will be non-uniform (Fig. 5d). Here we assume that the dropping region forms a triangle, such that the maximum drop rate, $-U_{s,max}$, will be equal to twice the mean drop rate. The maximum surface-drop rate can be converted into a slope-perpendicular drop rate, *C*, as follows (Fig. 5d):

$$C = (D_w - D_d)cos(\alpha) \tag{5}$$

If we assume that topographic warping results in minimal change in the peak elevation, we can estimate the topographic warp rate, V_{warp}, based on *C*:

$$V_{warp} = \frac{C}{\sin(\alpha)} = \frac{(D_w - D_d)cos(\alpha)}{\sin(\alpha)} = \frac{(D_w - D_d)}{\tan(\alpha)} \tag{6}$$

The predicted drainage-divide migration rates in the topographic-warp scenario (Eq. 6) are twice as high as in the topographic-shift scenario (Eq. 4) for a given difference in denudation rates across the range. This result is sensible, considering that the area of topographic change driven by topographic warping is assumed to be triangular, with half the area compared to the parallelogram-shaped region of topographic change driven by topographic shift (Fig. 5).

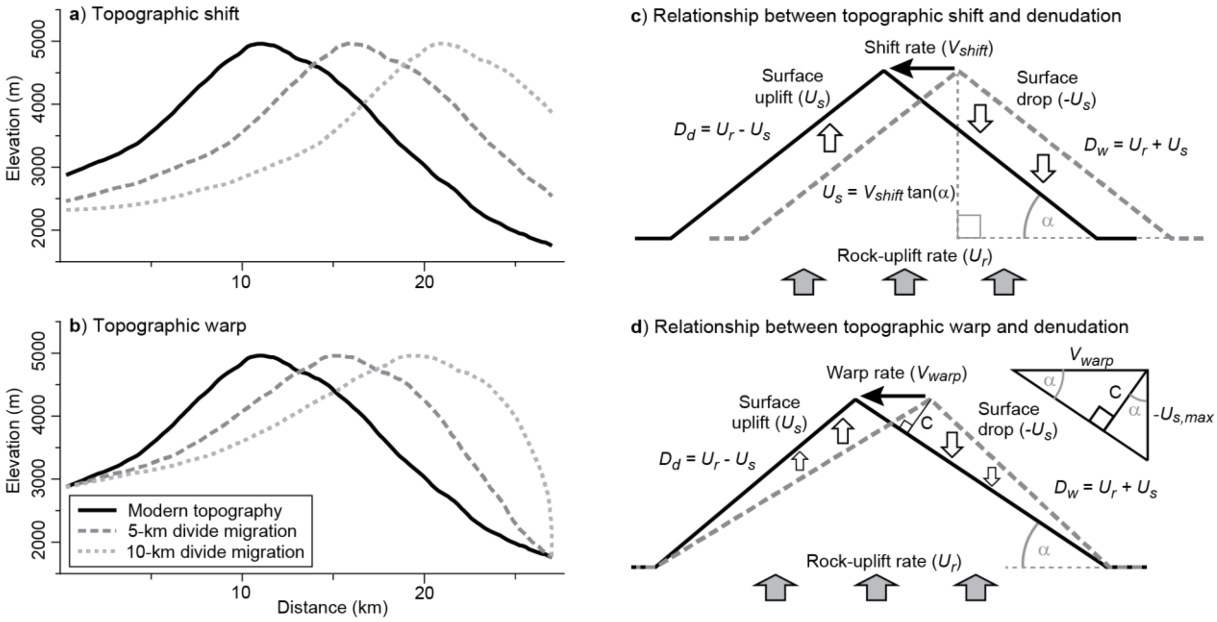

Figure 5. Changes in mean topography prescribed for Pecube thermal modeling, and simplified cartoons illustrating how the two topographic-evolution scenarios relate to denudation rates across the range. Pecube simulations assume drainage divide migration through time by either a) topographic shift, or b) topographic warp. Total magnitude of divide migration is either 5 or 10 km in both scenarios. Topographic shift is simulated by a simple translation of the modern topography, whereas topographic warp is simulated by warping modern topography with a sine function. All simulations end with the modern topography. c) Cartoon illustrating link between rate of topographic shift (V_{shift}) and denudation rates on both sides of the range. Surface uplift lowers the net denudation rate on the dry side (D_d), whereas surface drop increases the net denudation rate on the wet side (D_w). d) Link between rate of drainage-divide migration through topographic warp (V_{warp}) and denudation on both sides of the range.

4. Results

4.1. The influence of drainage-divide migration on thermochronometer age patterns

Our first set of thermal-kinematic models show that both topographic shift (Fig. S2) and topographic warp (Fig. S3) result in patterns of thermochronometric ages that are similar to those presented in the 2-D models by Stüwe and Hintermüller (2000) and Olen et al. (2012): ages on the wet side of the range tend to be younger than those on the dry side at similar elevations, and the age-elevation relationship is steeper (more similar ages at different elevations) on the dry side of the range than on the wet side. A larger separation in ages between the two flanks occurs with increasing divide-migration rates. The results from topographic shift and topographic warp show broadly similar patterns; they differ primarily in age predictions at the lowest elevations, as this is where the difference between the two topographic evolution scenarios is greatest (Fig. 5a, b).

Both sets of results corroborate the finding by Stüwe and Hintermüller (2000) that differences in cooling-age patterns (or plots of age versus elevation) on the wet and dry sides of the range should be apparent when lateral migration rates are at least ca. 2 mm/yr (2 km/Myr). If divide migration occurs closer to the present day, the range of ages and lateral separation of ages in the age-elevation plot is greater than if the migration occurred earlier in the exhumation history (compare Fig. S2e and f, Fig. S2g and h; Fig. S3e and f; Fig. S3g and h). This effect is most pronounced for the fastest divide-migration rates explored in these synthetic tests (4 km/Myr).

These tests illustrate that the timing, magnitude, and rate of drainage-divide migration all play a role in determining the predicted age patterns.

4.2. Investigating the topographic evolution of the Sierra de Aconquija

Following these generic models, we next assess which landscape-evolution scenarios are consistent with the thermochronologic ages available from the Sierra de Aconquija. Two sets of simulations yield high misfits when compared to the cooling ages: (1) steady topography and (2) topography that grows upward and shifts laterally simultaneously, examples of which are included in the Supplementary Information (Figs. S4 and S5). Both sets of simulations predict little to no lateral separation of AFT ages between the wet and dry sides in age-elevation plots. In the case of simultaneous surface uplift and drainage-divide migration, surface uplift acts to counteract rock exhumation, leading to less deflection of near-surface isotherms and a reduced difference in ages on either side of the range, in agreement with results by Stüwe and Hintermüller (2000).

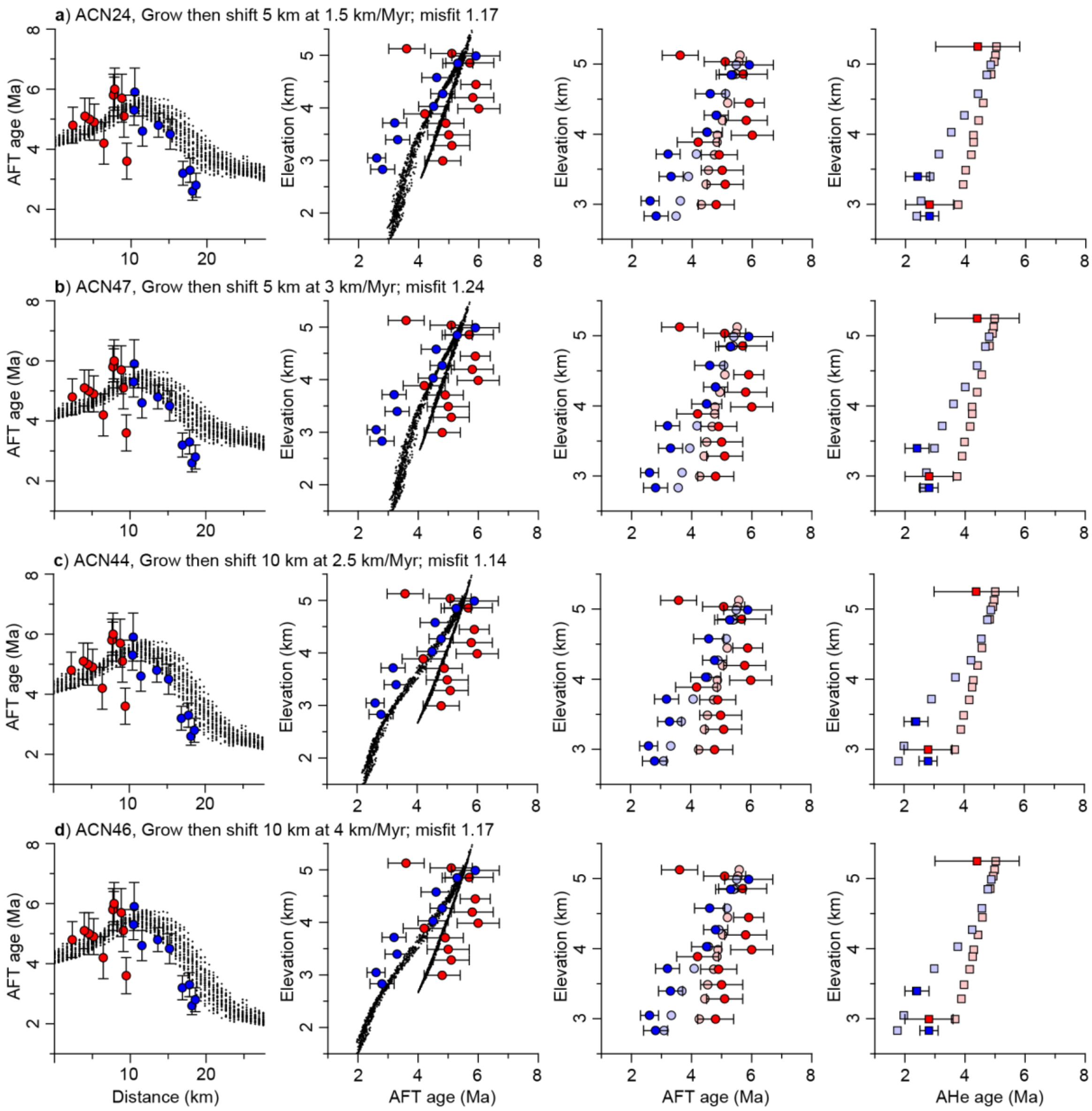

Figure 6. Comparison of observed AFT and AHe ages with ages predicted from simulations in Pecube, with initial growth of topography followed by a shift to the northwest. a) and b) simulate 5 km of total shift, with a rate of 1.5 km/Myr (a) or 3 km/Myr (b). c) and d) simulation of 10 km of total shift, at a rate of 2.5 km/Myr (c) or 4 km/Myr (d). Dark red and blue points in each plot show reported AFT or AHe ages. Black points show predicted AFT ages throughout model domain. Light blue and light red points show AFT or AHe model-predicted ages at the same location as the reported data. Uncertainties shown for reported ages are +/- 1σ.

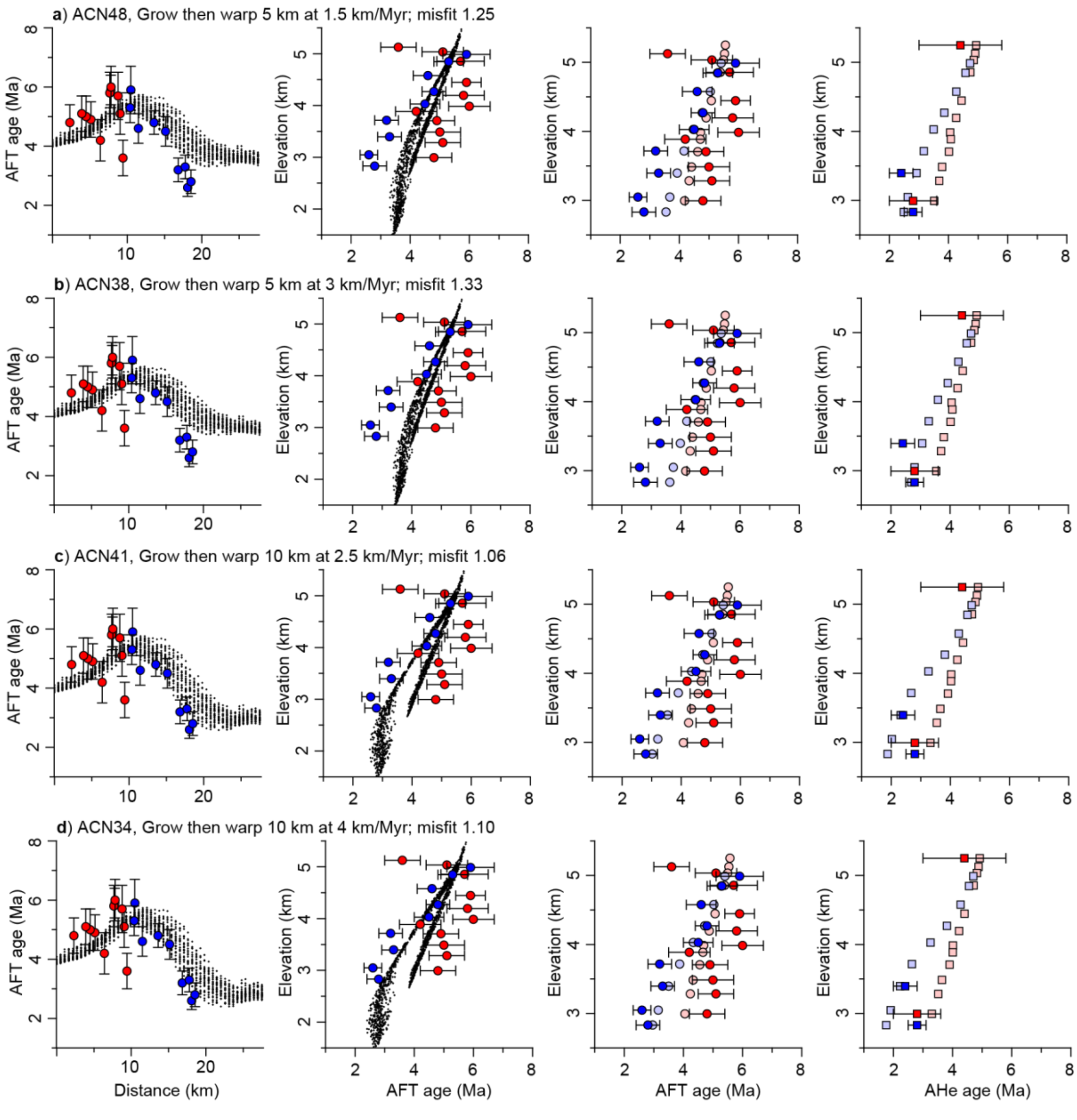

Figure 7. Comparison of observed AFT and AHe ages with ages predicted from simulations in Pecube, with initial growth of topography followed by topographic warping leading to drainage-divide migration to the northwest. a) and b) simulation of 5 km of total warp, with a rate of 1.5 km/Myr (a) or 3 km/Myr (b). c) and d) simulation of 10 km of total warp, at a rate of 2.5 km/Myr (c) or 4 km/Myr (d). All symbols and uncertainties are as in Fig. 6.

Scenarios that yield low misfit values and predict age patterns that broadly match those observed involve initial vertical topographic growth followed by divide migration through either topographic shifting (Fig. 6) or topographic warping (Fig. 7). To obtain cooling and topographic-evolution scenarios that are consistent with both the thermochronologic ages and independent geologic constraints, the initial rock-uplift rate must be rapid (ca. 2.0 to 2.5 km/Myr), followed by slower rates after a few million years (ca. 0.5 km/Myr). In both sets of simulations, scenarios with 10 km of total divide migration tend to create larger separations of AFT ages in age-elevation space (Figs. 6, 7) as well as lower misfit values when assessing all available thermochronometers (Fig. 8), than scenarios with 5 km of total divide migration. However, misfits for the topographic-shift scenarios comprise a wider range, including much higher values, compared to topographic-warp scenarios. The scenarios with the lowest misfits overall ($\chi^2 \leq 1.1$) comprise 10 km of topographic shift at 2.5 km/Myr or 10 km of topographic warp at rates of 3.0 to 5.0 km/Myr (Fig. 8).

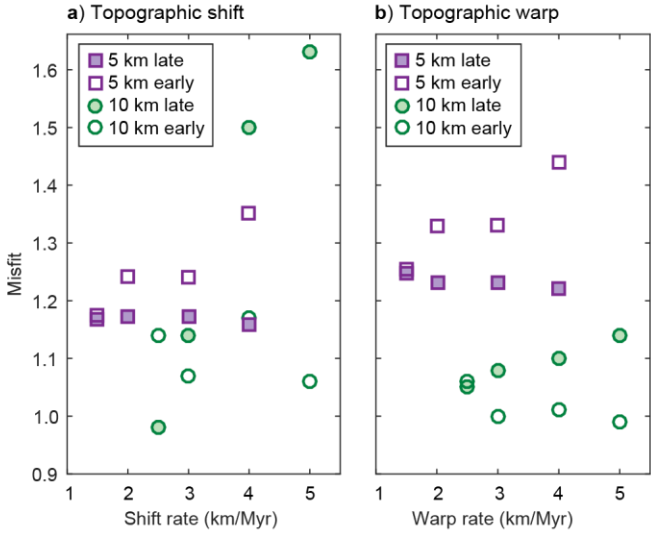

Figure 8. Misfit values comparing all available cooling ages with predicted ages from Pecube simulations involving a) topographic shift or b) topographic warp.

4.3. Investigating structural evolution of the Sierra de Aconquija

We have shown above that the thermochronometric age patterns reported from the Sierra de Aconquija can be explained by a morphologic scenario involving surface uplift followed by ca. 10 km of divide migration, but the question remains whether these patterns could also result from structural evolution of the range. Based on the geometry of structures bounding the Aconquija basement block to the west and east, we explored whether motion prescribed purely on the west-vergent structure or sequentially first on the west-vergent structure then on an east-vergent structure could reasonably fit the reported thermochronometric ages. In our explored scenarios, motion on the west-vergent structure (simulated as in Fig. 4c) is initially rapid (2.0 – 2.5 km/Myr) and slows down to 0.2 – 0.5 km/Myr after a few Myr, to be consistent with the slowdown in rock-uplift rate required by the combined geological constraints and thermochronologic data. As in the topographic-evolution scenarios, the model starts at 6 Ma with flat topography at 500 m elevation, and the topography grows after rock uplift has started. When imposing motion only on the west-vergent structure, there is little separation of AFT ages across the range (Fig. 9a). Hence, we consider this scenario unrealistic.

Next, we first imposed rapid (2.0 km/Myr) exhumation on the west-vergent structure, followed by a lateral gradient in rock uplift starting at 2.5 Ma (from 0 on the west side of the range to 0.8 km/Myr on the east side; Fig. 4d). This latter stage of deformation is meant to simulate motion along one or both of the back-thrusts that Löbens et al. (2013) inferred to be active within the last several million years. The resulting age pattern provides a very good match to the reported AFT and AHe ages (misfit value of 0.85, Fig. 9b).

A final thermo-kinematic scenario we tested involved imposing motion only on the west-vergent structure, but also imposing 10 km of total drainage-divide migration through topographic warping at a rate of 3 km/Myr. That scenario also results in very good matches to the AFT and AHe ages, with a very low misfit of 0.89 (Fig. 9c).

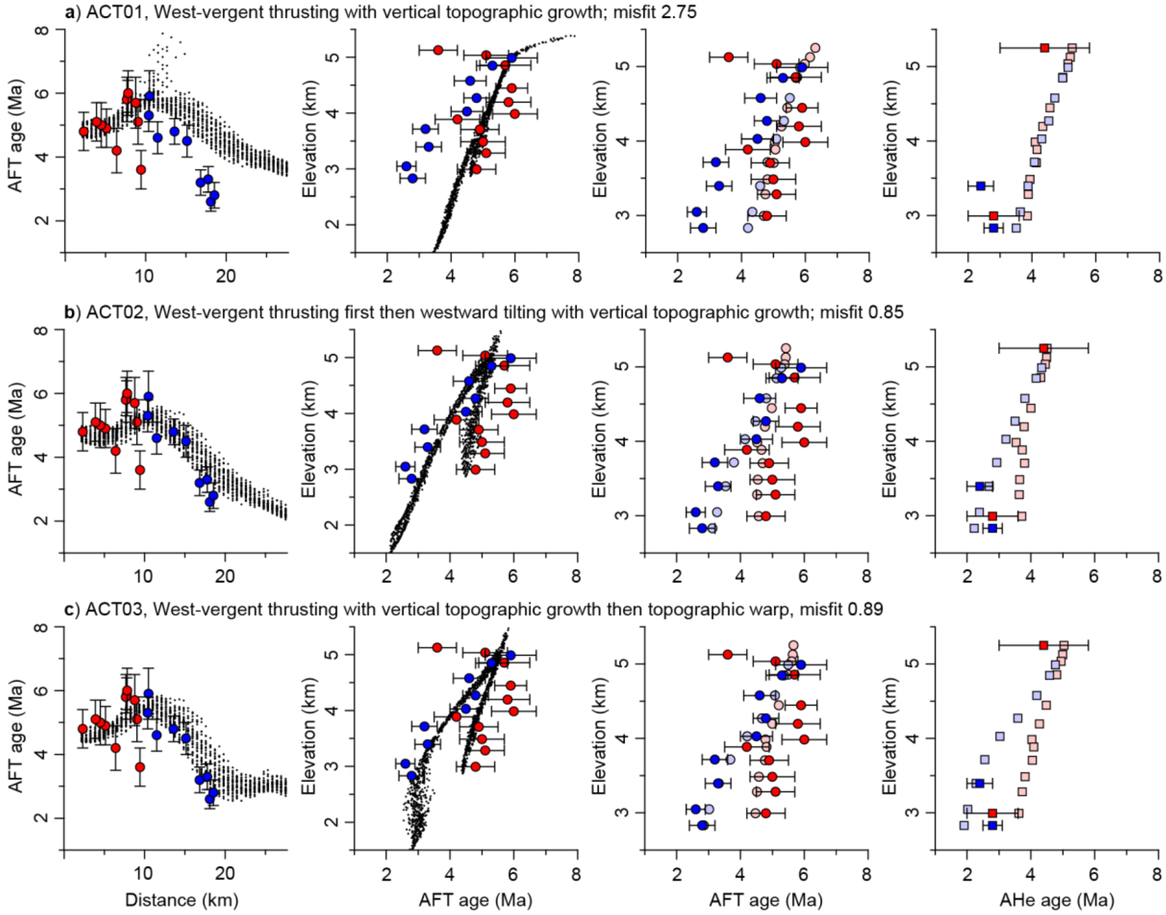

Figure 9. Comparison of observed AFT and AHe ages with ages predicted from thermal-kinematic simulations in Pecube, with rock-uplift accommodated by thrusting or tilting. a) Simulation of west-vergent thrusting at 2.0 km/Myr from 6 to 2.5 Ma, then slowing to 0.2 km/Myr since 2.5 Ma, with vertical topographic growth from 5.5 to 2.5 Ma. b) Simulation of west-vergent thrusting with same motion history as in a, combined with westward tilting since 2.5 Ma. c) Simulation of west-vergent thrusting with same motion history as in (a), but also including drainage-divide migration through topographic warping. Dark red and blue points in each plot show reported AFT or AHe ages. Black points show predicted AFT ages throughout model domain. Light blue and light red points show AFT or AHe model-predicted ages at the same location as the reported data. Uncertainties shown for reported ages are +/- 1σ.

Although small adjustments to the model parameters may produce slightly lower misfit values, considering the relatively high uncertainties on the thermochronological data, those scenarios cannot be distinguished from the ones presented above. As a result, we consider that structural evolution, or a combination of structural evolution and drainage-divide migration, can explain the data, but we do not attempt to precisely constrain the timing or rate of fault motion.

4.4. Catchment-average denudation rates

Catchment-average denudation rates are ca. 0.10 – 0.11 mm/yr on the dry side of the range (W1 through W3), and show a much wider range from ca. 0.07 to 1.46 mm/yr on the wet side (E1 though E4) (Table 1, Fig. 2a). One catchment (E4) has two estimated denudation rates, because the same catchment was sampled by Bookhagen and Strecker (2012) (their sample ARG11). The denudation rate reported in Table 1 for ARG11 has been recalculated with the same input parameters and procedure as the other samples.

Table 1

Information for detrital-sand samples used to calculated catchment-average denudation rates

Sample code (name)	Latitude (°S)	Longitude (°W)	Measured $^{10}Be/^{9}Be$[a] (± 1σ)	^{10}Be concentration[b] (atom g^{-1} ± 1σ)	Mean elevation (m)	Catchment avg. P_{sp}[c] (atom g^{-1} yr^{-1})	Catchment avg. P_{mc}[d] (atom g^{-1} yr^{-1})	T_{exp}[e] (yr)	Denudation rate (mm yr^{-1} ± 1σ)
E1 (MD16_79s)	-27.4546	-66.0257	1.10E-13 ± 5.09E-15	52700 ± 2450	2944	20.703	0.100	2084	0.256 ± 0.019
E2 (MD16_78s)	-27.4276	-65.9981	2.71E-13 ± 1.04E-14	135000 ± 5190	2188	14.138	0.083	8721	0.070 ± 0.005
E3 (MD16_122s)	-27.4010	-66.9794	1.43E-13 ± 6.84E-15	54300 ± 2630	3562	32.475	0.116	1437	0.380 ± 0.029
E4 (MD16_121s)	-27.3218	-66.9146	2.91E-14 ± 2.20E-15	13600 ± 1030	3213	31.665	0.108	415	1.476 ± 0.143
E4 (ARG11)[f]	-27.3218	-66.9146	n/a ± n/a	28700 ± 710	3213	30.008	0.108	876	0.665 ± 0.043
W1 (MD16_143s)	-27.2256	-66.2110	6.39E-13 ± 2.17E-14	246000 ± 8350	4300	41.658	0.135	4814	0.107 ± 0.007
W2 (MD16_76s)	-27.4010	-66.9794	3.06E-13 ± 1.13E-14	246000 ± 9090	4379	42.966	0.137	4644	0.110 ± 0.008
W3 (MD16_218s)	-27.1384	-66.1342	3.57E-13 ± 1.25E-14	291000 ± 10100	4471	45.703	0.140	5269	0.099 ± 0.007

[a] Standards used (nominal $^{10}Be/^{9}Be$ values) KN01-6-2 (5.35×10^{-13}), KN01-5-3 (6.320×10^{-12})

[b] Corrected for ^{10}Be added from ^{9}Be carrier and for batch-average $^{10}Be/^{9}Be$ blank of 1.27×10^{-15}

[c] Production rate of ^{10}Be from spallation; corrected for variations in paleomagnetic intensity (Charreau et al., 2019)

[d] Production rate of ^{10}Be from muon capture

[e] Equivalent exposure time, or "integration time" (von Blanckenburg, 2005)

[f] Sample reported by Bookhagen and Strecker (2012); not all information included in this table was reported for this sample

Because denudation rates on the wet side of the range are non-uniform, we can only calculate approximate divide-migration rates. Using the range of denudation rates from the two largest catchments that reach the divide on the wet side (catchments E3 and E4, with denudation rates of ca. 0.4 and 1.5 mm/yr), differences in denudation rates across the divide are ca. 0.3 to 1.4 mm/yr. Considering that the mean slope in the vicinity of the data collected is 11°, the estimated modern topographic-shift rate, V_{shift}, is 0.8 to 3.6 mm/yr (or 0.8 to 3.6 km/Myr) (Eq. 4). The same difference in denudation rates across the divide yields a topographic warp rate, V_{warp}, of 1.6 to 7.3 mm/yr (Eq. 6).

5. Discussion

The results from our thermal-kinematic modeling show that drainage-divide migration and structural evolution can both produce reasonable matches to the thermochronometric age patterns reported from the Sierra de Aconquija. Below, we consider how well each scenario corresponds with all available field observations, and where additional work may be needed to better test the viability of the different scenarios.

5.1. Structural evolution of the Sierra de Aconquija

Cristallini et al. (2004) suggested that uplift of the Sierra de Aconquija occurred primarily as a result of motion along the major west-vergent structure that they suggested underlies the entire range (Fig. 4a). However, our simulations of exclusively west-vergent motion and vertical topographic growth produced poor fits to the available thermochronologic ages (Fig. 9a). To obtain reasonable matches to the ages with a structural evolution scenario, exhumation must initially be faster on the dry side of the range, and then switch to become faster along the back-thrusts on the wet side (Fig. 9b). Although this scenario produces very good matches to the data and low misfit values (Fig. 9b), we question whether several kilometers of motion along the back-thrusts is reasonable. In the seismic lines interpreted by Cristallini et al. (2004), the back-thrust bounding the Aconquija basement block to the east (Fault B2 in Fig. 4a) barely offsets the Neogene sediments deposited above it. Therefore, it does not appear to contribute substantially to the required deformation of several km. If motion were instead focused along the back-thrust inferred by Löbens et al. (2013) to exist mid-way up the eastern flank of the range (Fault B1 in Fig. 4a), based on the anomalously old age of ACON29, we would expect to see a clear geomorphic expression of that activity, such as a step-change in channel steepness values across the fault. However, there is no apparent change in river steepness values across the zone where Löbens et al. (2013) suggested the fault should intersect the surface (Fig. 2d). Additional samples from the lower slopes of the Sierra de Aconquija would help to better test this scenario, and also allow an assessment of whether the reported old age for ACON29 is reliable. Thus, although we can match the remaining thermochronologic data well by imposing a purely structural evolution history, that scenario does not appear to be supported by the stratigraphic and geomorphic observations.

A caveat to this conclusion is that the deformation field that we imposed in our thermal-kinematic modeling is simplified. Thermal-mechanical modeling would enable a more realistic simulation of the deformation field in regions where back-thrusts develop, and could be used to assess which boundary conditions lead to the inferred structural evolution. Such models would also enable explorations into potential feedbacks between topographic and structural evolution in a region that experiences orographic precipitation. Furthermore, strong differences in erodibility along the flanks of the Sierra de Aconquija may mask changes in steepness associated with active thrusting. Although such a step-change to lower erodibility in the hanging wall of the fault (needed to offset the increase in steepness expected in areas of faster rock uplift) seems unrealistic in this region of uniform lithology, we cannot fully rule it out.

5.2. Drainage-divide migration at the Sierra de Aconquija

Divide migration at a rate of ca. 2 to 5 km/Myr, which has persisted over several millions of years through either topographic warping or shifting, can explain the pattern of thermochronologic ages across the Sierra de Aconquija (Figs. 6-8). These results are consistent with the estimated divide-migration rates of ca. 1 to 7 km/Myr based on the difference in modern, millennial-scale denudation rates between the wet and dry sides of the range. Together, these results imply that links between orographic rainfall and erosion that are observed today in the Central Andes (Bookhagen and Strecker, 2012) and appear to have persisted over the last several Myr (Pingel et al., 2019) could have had a substantial impact on the topographic evolution of individual ranges.

The available thermochronometric data do not allow us to distinguish whether the Sierra de Aconquija was affected by either topographic shifting or topographic warping: both sets of topographic simulations can yield similarly low misfits to the data (Fig. 8). However, in the case of topographic shifting, one would expect denudation rates to be near-uniform across the wet flank of the range, whereas topographic warping would lead to lower denudation rates on the lower slopes on the wet side, compared to the upper slopes (Fig. 5c and d). Based on our ^{10}Be-derived denudation rates, catchments on the wet side that are farther south have lower denudation rates, which might result from partial blocking of rainfall by a topographic rise to the east of the sampling points E1, E2, and E3 (Fig. 2a). Despite that north-to-south variation in denudation rates, catchment-average denudation rates on the wet side are higher for the catchments that reach up to the drainage divide (E3 and E4; Fig. 2a) compared to those that only drain the lower slopes of the range (E1 and E2; Fig. 2a), thus providing support for drainage-divide migration through topographic warping.

The modern denudation rates do not exclude the possibility of some degree of wholesale topographic shift, which would require activation of new structures to accommodate a lateral shift in topography. Although it is difficult to map structures along the densely vegetated, lower eastern slopes of the Sierra de Aconquija, the inferred activation of a back-thrust mid-way up the slope (Löbens et al., 2013) could be the expression of topographic migration toward the west. On the dry west flank of the range, the disruption of Quaternary fan surfaces that drape across the toe of the range (Strecker et al., 1989) provides support for active westward (outward) propagation of structures. Further evaluation of this possibility would require coupled thermal-mechanical and surface-process modeling.

5.3. Combining structural deformation and drainage-divide migration

In our initial models of drainage-divide migration, we imposed a uniform rock-uplift field throughout the model domain. A structural implication of spatially uniform rock uplift is that high-angle structures bounding the Sierra de Aconquija on the west and east sides are simultaneously active at similar rates. For the reasons described in section 5.1, we question the viability of km-scale motion on the east-vergent structures along the eastern side of the range (Faults B1 and B2 in Fig. 4a). Another possibility is that motion has been accommodated predominantly along the major west-vergent structure, but topography was also affected by drainage-divide migration. Our simulation of this combined kinematic and climatic forcing of landscape evolution produces very good fits to the observed thermochronologic ages, and is consistent with the available stratigraphic and geomorphic constraints (Fig. 9c). For this reason, we consider a scenario of structural evolution as envisioned by Cristallini et al. (2004), with motion predominantly occurring along the west-vergent structure, together with drainage-divide migration through topographic warping, to be the scenario most likely to capture the landscape evolution of the region.

Drainage-divide asymmetry may not only be caused by asymmetric rainfall patterns, but can also result from horizontal rock advection and/or asymmetric uplift, with the divide migrating toward the side of the mountain range with higher uplift rate or in the direction of rock advection (e.g., Willett et al., 2001; He et al., 2021). The topographic asymmetry towards the west observed at the Sierra de Aconquija is both qualitatively and quantitatively consistent with the model predictions by He et al. (2021) for an uplift gradient in the case of a single west-vergent fault (i.e., Fig. 9a). However, because our simulations of west-vergent thrusting combined with drainage-divide migration require a substantial slowing of the thrusting rate in the last few million years (from ca. 2.5 to ca. 0.5 km/Myr), the degree of tectonically induced asymmetry in this case should have been reduced, thus driving eastward drainage-divide migration in the last few million years. This scenario is inconsistent with geomorphic observations (Bonnet, 2009) and the ^{10}Be derived denudation-rate data, which suggest ongoing westward drainage-dive migration at the Sierra de Aconquija (Fig. 9a). The alternative, purely structural-evolution scenario (i.e., with no drainage-divide migration, thrusting first on the west-vergent structure and then on an east-vergent back-thrust; Fig. 9b), would also imply drainage-divide migration toward the east since the onset of eastward thrusting, which is again inconsistent with evidence for ongoing westward migration. Although some of the modern asymmetry of the range could result from non-uniform rock uplift, ongoing westward divide migration at the Sierra de

Aconquija supports the scenario of drainage-divide migration combined with west-vergent thrusting, with drainage-divide migration predominantly driven by orographic rainfall.

5.4. Implications of drainage-divide migration on interpretations of thermochronometric data

Despite the growing recognition of the potential for divide migration to affect landscape evolution, there has been little consideration of how lateral evolution of topography may affect interpretations of thermochronometric data, apart from theoretical numerical simulations (Stüwe and Hintermüller, 2000; Olen et al., 2012). Our simulations of drainage-divide migration at rates of 3 to 5 km/Myr provide good fits to thermochronology data that span both sides of the Sierra de Aconquija, with the wet side of the range yielding younger ages overall compared to the dry side of the range. If data from only one side of a range that has experienced asymmetric exhumation and drainage-divide migration were considered when interpreting its exhumation history, a biased picture could emerge. Such a situation provides another example of spatial variation in cooling ages that can be interpreted erroneously (Schildgen et al., 2018).

Whether the topography of a range has experienced substantial lateral changes in response to asymmetric precipitation could depend strongly on rock-exhumation pathways. At the Sierra de Aconquija and several other ranges within the broken foreland of the Central Andes, high-angle reverse faults bounding the ranges drive steep rock trajectories. This inference is supported by a preserved paleosurface atop the Cumbres Calchaquies, a range just north of Aconquija, which shows minimal tilting, despite having experienced ca. 4 km of surface uplift since the time it was exhumed from beneath foreland sediments (Sobel and Strecker, 2003; Zapata et al., 2020). Considering our results from the Sierra de Aconquija, these ranges are likely each affected by substantial drainage-divide migration. In other mountain belts, horizontal advection of rocks may offset asymmetric erosion patterns, and eventually lead to steady-state topography. For example, in the southern Alps of New Zealand, exhumation along the transpressional Alpine fault leads to steeper exhumation pathways along the western side of the range, which is also much wetter compared to the eastern side (e.g., Willett, 1999). There, the onset of orographic precipitation at ca. 7 Ma has led to a significant increase in exhumation rates (Lang et al., 2020), consistent with modeling expectations (Zavala et al., 2020), but has not modified the topographic asymmetry of a mountain range that appears to be dominated by lateral rock advection.

6. Conclusions

Orographic rainfall, and its related impact on landscape evolution, can have a substantial effect on age patterns recorded by low-temperature thermochronometers. We examined this effect at the Sierra de Aconquija in the southern Central Andes, which has been subjected to a strong and persistent orographic rainfall gradient. Based on three-dimensional thermal-kinematic modeling, we found that several scenarios of landscape evolution (structural evolution, drainage-divide migration, and a combination of both) can produce reasonable fits to the thermochronologic ages reported from the wet and dry flanks of the range. By considering these scenarios in the context of our new ^{10}Be-derived catchment-average denudation rates and geologic/geomorphic constraints on the structural evolution of the region, we conclude that the scenario most consistent with the full set of empirical data comprises initial topographic growth due to west-vergent thrusting, followed by drainage-divide migration through topographic warping at a rate of several km/Myr, driven predominantly by orographic rainfall. Mountain ranges that are characterized by steep rock trajectories (or where active tectonics has waned) and that experience significant orographic precipitation patterns will be particularly sensitive to drainage-divide migration. In such settings, cooling-age patterns can be interpreted in multiple ways, and careful integration of independent data is required to assess the most realistic tectonic and topographic-evolution scenarios.

Acknowledgments

T.S. acknowledges support from the Helmholtz W2/W3 Professorinnen Program (W2_W3-0072). P.v.d.B. and M.D. were supported by fellowships from the Alexander von Humboldt Foundation, and M.D. also by an Early Career Research grant from the British Society for Geomorphology that supported sample collection. E.O. was supported by the Deutsche Forschungsgemeinschaft (DFG) and the Federal State of Brandenburg within the International Research Training Group IGK2018 “SuRfAce processes, TEctonics and Georesources: The Andean foreland basin of Argentina” (STRATEGy DFG 373/34-1). We thank W. Düsing for help with sample collection and processing. The Deutsches Zentrum für Luft- und Raumfahrt (DLR) provided TanDEM-X digital elevation data through grant DEM_GEOL1915 awarded to T.S. and M.D. We are grateful to two anonymous reviewers whose detailed comments helped us to improve the clarity and presentation of our work.

References

Beaumont, C., Fullsack, P., Hamilton, J., 1992. Erosional control of active compressional orogens, in: McClay, K.R. (Ed.), Thrust Tectonics. Springer, pp. 1–18. https://doi.org/10.1007/978-94-011-3066-0

Bonnet, S., 2009. Shrinking and splitting of drainage basins in orogenic landscapes from the migration of the main drainage divide. *Nat. Geosci.* 2, 766-771. https://doi.org/10.1038/ngeo666

Bookhagen, B., Strecker, M.R., 2008. Orographic barriers, high-resolution TRMM rainfall, and relief variations along the eastern Andes. *Geophys. Res. Lett.* 35(6), https://doi.org/10.1029/2007GL032011

Bookhagen, B., Strecker, M.R., 2012. Spatiotemporal trends in erosion rates across a pronounced rainfall gradient: Examples from the southern Central Andes. *Earth. Planet. Sci. Lett.* 327-328, 97-110. https://doi.org/10.1016/j.epsl.2012.02.005

Bossi, G.E., Georgieff, S.M., Ibañez, L.M., Muruaga, C.M., 2001. Cenozoic evolution of the intramontane Santa María basin, Pampean Ranges, northwestern Argentina. *J. S. Am. Earth Sci.* 14(7), 725-734. https://doi.org/10.1016/S0895-9811(01)00058-X

Braun, J., van der Beek, P., Valla, P., Robert, X., Herman, F., Glotzbach, C., Pedersen, V., Perry, C., Simon-Labric, T., Prigent, C., 2012. Quantifying rates of landscape evolution and tectonic processes by thermochronology and numerical modeling of crustal heat transport using PECUBE. *Tectonophysics* 524–525, 1–28. https://doi.org/10.1016/j.tecto.2011.12.035

Charreau, J., Blard, P.-H., Zumaque, J., Martin, L.C.P., Delobel, T., Szafran, L., 2019. Basinga: A cell-by-cell GIS toolbox for computing basin average scaling factors, cosmogenic production rates and denudation rates. *Earth Surf. Proc. Landf.*, 44(12), 2349-2365. https://doi.org/10.1002/esp.4649

Cristallini, E.O., Cominguez, A.H., Ramos, V.A., Mercerat, E.D., 2004. Basement double-wedge thrusting in the northern Sierras Pampeanas of Argentina (27ºS) — Constraints from deep seismic reflection, in: McClay, K.R. (Ed.), Thrust Tectonics and Hydrocarbon Systems, AAPG Memoir 82. American Association of Petroleum Geology, pp. 65–90.

D'Arcy, M., Schildgen, T.F., Strecker, M.R., Wittmann, H., Duesing, W., Mey, J., Tofelde, S., Weissmann, P., Alonso, R.N., 2019. Timing of past glaciation at the Sierra de Aconquija, northwestern Argentina, and throughout the Central Andes. *Quat. Sci. Rev.* 204, 37-57. https://doi.org/10.1016/j.quascirev.2018.11.022

D'Arcy, M., Whittaker, A.C., 2014. Geomorphic constraints on landscape sensitivity to climate in tectonically active areas. *Geomorphology* 204, 366-381. https://doi.org/10.1016/j.geomorph.2013.08.019

Dahlen, F.A., Suppe, J., 1988. Mechanics, growth, and erosion of mountain belts, in: Clark, S.P., Jr., Burchfiel, B.C., Suppe, J. (Eds.), Processes in Continental Lithospheric Deformation, GSA Special Papers, 218. Geological Society of America, pp. 161–178.

Dahlquist, M.P., West, A.J., Li, G., 2018. Landslide-driven drainage divide migration. *Geology*, 46(5), 403-406. https://doi.org/10.1130/G39916.1

Ehlers, T.A., Farley, K.A., Rusmore, M.E., Woodsworth, G.J., 2006. Apatite (U-Th)/He signal of large-magnitude accelerated glacial erosion, southwest British Columbia. *Geology*, 34 (9), 765–768. https://doi .org /10 .1130 /G22507.1

Frisch, W., Kuhlemann, J., Dunkl, I., Brügel, A., 1998. Palinspastic reconstruction and topographic evolution of the Eastern Alps during late Tertiary tectonic extrusion. *Tectonophysics* 297(1-4), 1-15. https://doi.org/10.1016/S0040-1951(98)00160-7

Gilbert, G.K., 1877. Report on the Geology of the Henry Mountains (Utah), Survey of the Rocky Mountains Region Rep., United States Geological Survey, Washington, D.C.

Grier, M.E., Salfity, J.A., Allmendinger, R.W., 1991. Andean reactivation of the Cretaceous Salta rift, northwestern Argentina. *J. S. Am. Earth Sci.* 4(4), 351-372. https://doi.org/10.1016/0895-9811(91)90007-8

Han, J., Gasparini, N., Johnson, J.J., 2015. Measuring the imprint of orographic rainfall gradients on the morphology of steady-state numerical fluvial landscapes. *Earth Surf. Proc. Landf.* 40(10), 1334-1350. https://doi.org/10.1002/esp.3723

He, C., Yang, C.-J., Turowski, J.M., Rao, G., Roda-Boluda, D.C., Yuan, X.-P., 2021. Constraining tectonic uplift and advection from the main drainage divide of a mountain belt. *Nat. Commun.* 12, 544. https://doi.org/10.1038/s41467-020-20748-2

Hu, K., Fang, X., Ferrier, K., Granger, D., Zhao, Z., Ruetenik, G.A., 2021. Covariation of cross-divide differences in denudation rate and χ: Implications for drainage basin reorganization in the Qilian Shan, northeast Tibet. *Earth Planet Sci. Lett.*, 562, 116812. https://doi.org/10.1016/j.epsl.2021.116812

Iaffa, D.N., Sàbat, F., Muñoz, J.A., Carrera, N., 2013. Basin fragmentation controlled by tectonic inversion and basement uplift in Sierras Pampeanas and Santa Bárbara System, northwest Argentina. *Geol. Soc. Lond. Spec. Pub.* 377, 101–117. https://doi.org/10.1144/sp377.13

Kleinert, K., Strecker, M.R., 2001. Climate change in response to orographic barrier uplift: Paleosol and stable isotope evidence from the late Neogene Santa María basin, northwestern Argentina. *Geol. Soc. Am. Bull.* 113(6), 728-742. https://doi.org/10.1130/0016-7606(2001)113<0728:CCIRTO>2.0.CO;2

Lang, K.A., Glotzbach, C., Ring, U., Kamp, P.J.J., Ehlers, T.A., 2020. Linking orogeny and orography in the Southern Alps of New Zealand: New observations from detrital fission-track thermochronology of the Waiho-1 borehole. *Earth Planet. Sci. Lett.* 552, 116586. https://doi.org/10.1016/j.epsl.2020.116586

Löbens, S., Sobel, E.R., Bense, F.A., Wemmer, K., Dunkl, I., Siegesmund, S., 2013. Refined exhumation history of the northern Sierras Pampeanas, Argentina. *Tectonics* 32(3), 453-472. https://doi.org/10.1002/tect.20038

Mark, C., Cogné, N., Chew, D., 2016. Tracking exhumation and drainage divide migration of the Western Alps: A test of the apatite U-Pb thermochronometer as a detrital provenance tool. *Geol. Soc. Am. Bull.* 128(9-19), 1439-1460. https://doi.org/10.1130/B31351.1

Mey, J., D’Arcy, M., Schildgen, T.F., Egholm, D.L., Wittmann, H., Strecker, M.R., 2020. Temperature and precipitation in the southern Central Andes during the last glacial maximum, Heinrich Stadial 1, and the Younger Dryas. *Quat. Sci. Rev.* 248, 106592. https://doi.org/10.1016/j.quascirev.2020.106592

Mortimer, E., Carrapa, B., Coutand, E., Schoenbohm, L., Sobel, E.R., Gomez, J.S., Strecker, M.R. 2007. Fragmentation of a foreland basin in response to out-of-sequence basement uplifts and structural reactivation: El Cajón-Campo del Arenal basin, NW Argentina. *Geol. Soc. Am. Bull.* 119 (5/6), 637-653. https://doi.org/10.1130/B25884.1

Olen, S.M., Ehlers, T.A., Densmore, M.S., 2012. Limits to reconstructing paleotopography from thermochronometer data. *J. Geophys. Res.* 117, F01024. https://doi.org/10.1029/2011jf001985

Oskin, M., Burbank, D.W., 2005. Alpine landscape evolution dominated by cirque retreat. *Geology* 33(12), 933-936. https://doi.org/10.1130/G21957.1

Penck, W., 1924. Die morphologische Analyse: ein Kapitel der physikalischen Geologie. J. Engelhorns nachf., Stuttgart, 283 p.

Pingel, H., Alonso, R.N., Mulch, A., Rohrmann, A., Sudo, M., Strecker, M.R., 2014. Pliocene orographic barrier uplift in the southern Central Andes. *Geology* 42(8), 691-694. https://doi.org/10.1130/G35538.1

Pingel, H., Mulch, A., Alonso, R.N., Cottle, J., Hynek, S.A., Poletti, J., Rohrmann, A., Schmitt, A.K., Stockli, D.F., Strecker, M.R., 2016. Surface uplift and convective rainfall along the southern Central Andes (Angastaco Basin, NW Argentina). *Earth Planet. Sci. Lett.* 40, 33-42. https://doi.org/10.1016/j.epsl.2016.02.009

Pingel, H., Schildgen, T., Strecker, M.R., Wittmann, H., 2019. Pliocene-Pleistocene orographic control on denudation in northwest Argentina. *Geology* 47(4), 359-362. https://doi.org/10.1130/G45800.1

Pingel, H., Strecker, M.R., Mulch, A., Alonso, R.N., Cottle, J., Rohrmann, A., 2020. Late Cenozoic topographic evolution of the Eastern Cordillera and Puna Plateau margin in the southern Central Andes (NW Argentina). *Earth Planet. Sci. Lett.* 535, 116112. https://doi.org/10.1016/j.epsl.2020.116112

Prince, P.S., Spotila, J.A., Henika, W.S., 2011. Stream capture as driver of transient landscape evolution in a tectonically quiescent setting. *Geology* 39(9), 823-826. https://doi.org/10.1130/G32008.1

Rohrmann, A., Sachse, D., Mulch, A., Pingel, H., Tofelde, S., Alonso, R.N., Strecker, M.R., 2016. Miocene orographic uplift forces rapid hydrological change in the southern central Andes. *Sci. Rep.* 6, 35678. https://doi.org/10.1038/srep35678

Schildgen, T.F., van der Beek, P.A., Sinclair, H.D., Thiede, R.C., 2018. Spatial correlation bias in late-Cenozoic erosion histories derived from thermochronology. *Nature* 559, 89-93. https://doi.org/10.1038/s41586-018-0260-6

Schwanghart, W., Scherler, D., 2020. Divide mobility controls knickpoint migration on the Roan Plateau (Colorado, USA). *Geology*, 48 (7), 698–702. https://doi .org /10 .1130 /G47054 .1

Simon-Labric, T., Brocard, G., Teyssier, C., van der Beek, P.A., Reiners, P.W., Shuster, D.L., Murray, K.E., Whitney, D.L., 2014. Low-temperature thermochronologic signature of range-divide migration and breaching in the North Cascades. *Lithosphere* 6(6), 473-482. https://doi.org/10.1130/L382.1

Sobel, E., Strecker, M.R., 2003. Uplift, exhumation and precipitation: tectonic and climatic control of Late Cenozoic landscape evolution in the northern Sierras Pampeanas, Argentina. *Bas. Res.* 15(4), 431-451. https://doi.org/10.1046/j.1365-2117.2003.00214.x

Strecker, M.R., Cerveny, P., Bloom, A.L., Malizia, D., 1989. Late Cenozoic tectonism and landscape development in the foreland of the Andes: Northern Sierras Pampeanas (26-28ºS), Argentina. *Tectonics* 8(3), 517-534, https://doi.org/10.1029/TC008i003p00517

Strecker, M.R., Hilley, G.E., Bookhagen, B., Sobel, E.R., 2011. Structural, geomorphic, and depositional characteristics of contiguous and broken foreland basins: Examples from the eastern flanks of the central Andes in Bolivia and NW Argentina, in: Busby, C., Azor, A. (Eds.), Tectonics of Sedimentary Basins: Recent Advances. Blackwell Publishing, pp. 508–521. https://doi.org/10.1002/9781444347166.ch25

Struth, L., Teixell, A., Owen, L.A., Babault, J., 2017. Plateau reduction by drainage divide migration in the Eastern Cordillera of Colombia defined by morphometry and ^{10}Be terrestrial cosmogenic nuclides. *Earth Surf. Proc. Landf.* 42(8), 1155-1170. https://doi.org/10.1002/esp.4079

Stüwe, K., Hintermüller, M., 2000. Topography and isotherms revisited: the influence of laterally migrating drainage divides. *Earth Planet. Sci. Lett.* 184(1), 287-303. https://doi.org/10.1016/S0012-821X(00)00315-0

von Blanckenburg, F., 2005. The control mechanisms of erosion and weathering at basin scale from cosmogenic nuclides in river sediment. *Earth Planet. Sci. Lett*., 237(3-4), 462-479. https://doi.org/10.1016/j.epsl.2005.06.030

Willett, S.D., 1999. Orogeny and orography: The effects of erosion on the structure of mountain belts. *J. Geophys. Res. Solid Earth*, 104(B12), 28957-28981. https://doi.org/10.1029/1999JB900248

Willett, S.D., Slingerland, R., Hovius, N., 2001. Uplift, shortening, and steady state topography in active mountain belts. *Am. J. Sci.* 301, 455–485. https://doi.org/10.2475/ajs.301.4-5.455

Whipple, K.X., 2009. The influence of climate on the tectonic evolution of mountain belts. *Nat. Geosci.* 2, 97-104. https://doi.org/10.1038/ngeo413

Zapata, S., Sobel, E. R., Del Papa, C., Glodny, J., 2020. Upper plate controls on the formation of broken foreland basins in the Andean retroarc between 26ºS and 28ºS: From Cretaceous rifting to Paleogene and Miocene broken foreland basins. *Geochem. Geophys. Geosys.* 21, e2019GC008876. https//doi.org/10.1029/2019GC008876

Zavala, V., Carretier, S., Bonnet, S., 2020. Influence of orographic precipitation on the topographic and erosional evolution of mountain ranges. *Basin Res.* 32, 1574–1599. https://doi.org/10.1111/bre.12443

Supplementary Material

Quantifying drainage-divide migration from orographic rainfall over geologic timescales: Sierra de Aconquija, southern Central Andes

T. F. Schildgen[*1,2], P. A. van der Beek[2], M. D'Arcy[3], D. Roda-Boluda[4], E. N. Orr[5], H. Wittmann[1]

1. GFZ German Research Centre for Geosciences, Potsdam, Germany
2. Institute for Geosciences, University of Potsdam, Potsdam, Germany
3. Department of Earth, Ocean and Atmospheric Sciences, University of British Columbia, Vancouver, Canada
4. Department of Earth Sciences, Vrije Universiteit Amsterdam, Amsterdam, Netherlands
5. School of Geographical Sciences, University of Bristol, Bristol, United Kingdom

[*]correspondence to: tschild@gfz-potdam.de

Using geologic constraints on landscape evolution to limit model parameter values

We considered the geologic constraints described in section 2 to constrain the range of parameter values we explored in our thermal-kinematic modeling. The geologic constraints can be summarized as follows:

1) Time-temperature histories derived from apatite fission track-length modeling (Sobel and Strecker, 2003) indicate rapid cooling starting at ca. 6 Ma, and slower cooling between 4 and 2 Ma;
2) Basement exhumation started no later than ca. 4 Ma, based on the presence of basement-derived conglomerates within the ca. 5 to 3.4 Ma Andahuala Formation (Strecker et al., 1989), and the dominance of basement-derived conglomerates within the 3.4 to 3.0 Ma Corral Quemado Formation (Strecker et al., 1989; Bossi et al., 2001);
3) Stable-isotope values within the Santa María Basin to the west (Kleinert and Strecker, 2001) indicate at least 2000 m of elevation had developed by 1.4 Ma.

These geologic constraints on the evolution of the Sierra de Aconquija imply rapid unroofing of at least 1000 m of sediment starting at ca. 6 Ma with minimal associated surface uplift. Exposure of less erodible basement between ca. 5 and 4 Ma led to a decrease in exhumation rates and simultaneous rapid topographic growth (Sobel and Strecker, 2003) at a rate of ca. 1 to 2 mm/yr. Because surface uplift cannot exceed rock uplift, this geologic constraint defines a minimum rock-uplift rate at the start of the modeling. Considering that the thermochronologic ages furthermore require exhumation at a rate of ca. 1 mm/yr to occur between ca. 5 and 3 Ma (based on the best-fit average slope of the age-elevation relationships), the total rock uplift must be ca. 2 to 3 mm/yr in the first few million years of the model runs. However, if we impose a rock-uplift rate of 2 to 3 mm/yr until 0 Ma in the simulation, the predicted thermochronologic ages are much too young compared to the observed ages. Hence, the rock-uplift rates must decelerate after the first few million years of the simulations that include topographic growth.

In our model simulations that did not involve any initial topographic growth, we found that rock-uplift rates of ca. 1.0 mm/yr consistently yielded the lowest misfit values, in line with our predictions based on the best-fit slope of the age-elevation relationship. For simulations that involved initial topographic growth followed by drainage-divide migration, we found that rock-uplift rates of 2.3 to 2.5 mm/yr in the first few million years of the simulation, followed by a slower rock-uplift rate of 0.4 to 0.5 mm/yr starting at 3.5 Ma, consistently yielded the lowest misfit values. Values different from these produced age-elevation relationships with slopes that were a poor match to the data and/or yielded ages that were systematically too young or too old compared to the reported ages.

^{10}Be sample preparation, measurement, and denudation-rate calculation

Samples were processed at the GeoForschungsZentrum (GFZ) Potsdam HELGES laboratory following standard procedures (Nishiizumi et al., 1989; von Blanckenburg et al., 2004; Wittmann et al., 2016). Quartz from the 250-700 µm size fraction was concentrated by removing magnetic fractions followed by HCl and H_2O_2 treatment to dissolve carbonates and organic material. Samples were then leached in a 2%HF/2%HNO_3 solution a minimum of three times for 12h each in an ultrasonic bath to dissolve non-quartz minerals and remove meteoric ^{10}Be. Column chemistry and target preparation followed procedures described by von Blanckenburg et al. (2004) and Wittmann et al. (2016). A carrier of 150 µg of ^{9}Be was added to each sample prior to quartz digestion and isolation of $Be(OH)_2$ via column chemistry. Be was then oxidized to BeO and prepared as targets for analysis by accelerator mass spectrometry (AMS). AMS measurements were performed at the University of Cologne, Germany. Measured Be isotope values were normalized to the standards KN01-6-2 and KN01-5-3 with a nominal ^{10}Be/^{9}Be ratio of $5.35*10^{-13}$ and $6.32*10^{-12}$, respectively. Concentration corrections were performed for each sample based on the blank ratios processed with the same batch of samples.

After obtaining the ^{10}Be concentration in our samples, we calculated catchment-average denudation rates with the ArcGIS toolbox Basinga (Charreau et al., 2019). Catchment-average ^{10}Be production rates were scaled with the Lal/Stone model from a global average sea-level high-latitude production rate of 4.11 atoms g^{-1} yr^{-1} based on the ERA40 atmosphere model (Martin et al., 2017) and corrected for variations in paleomagnetic intensity through time. We did not correct for topographic shielding, following DiBiase (2018), nor for ice/snow cover. Justification for the latter is based on the integration times of the samples, which do not extend back to the last glacial period (see Results), and also considering that the thin, transient snow cover that occurs on the uppermost slopes will have an insignificant impact on catchment-average production rates.

Author Contributions

Conceptualization: T.S., P.v.d.B., D.R.B., M.D.; Data analysis and modeling: P.v.d.B., T.S.; Funding acquisition: T.S., M.D.; Sample collection and processing: M.D., T.S., D.R.B., E.O., H.W.; Visualization: T.S., P.v.d.B., with feedback from all authors; Writing & editing: all authors.

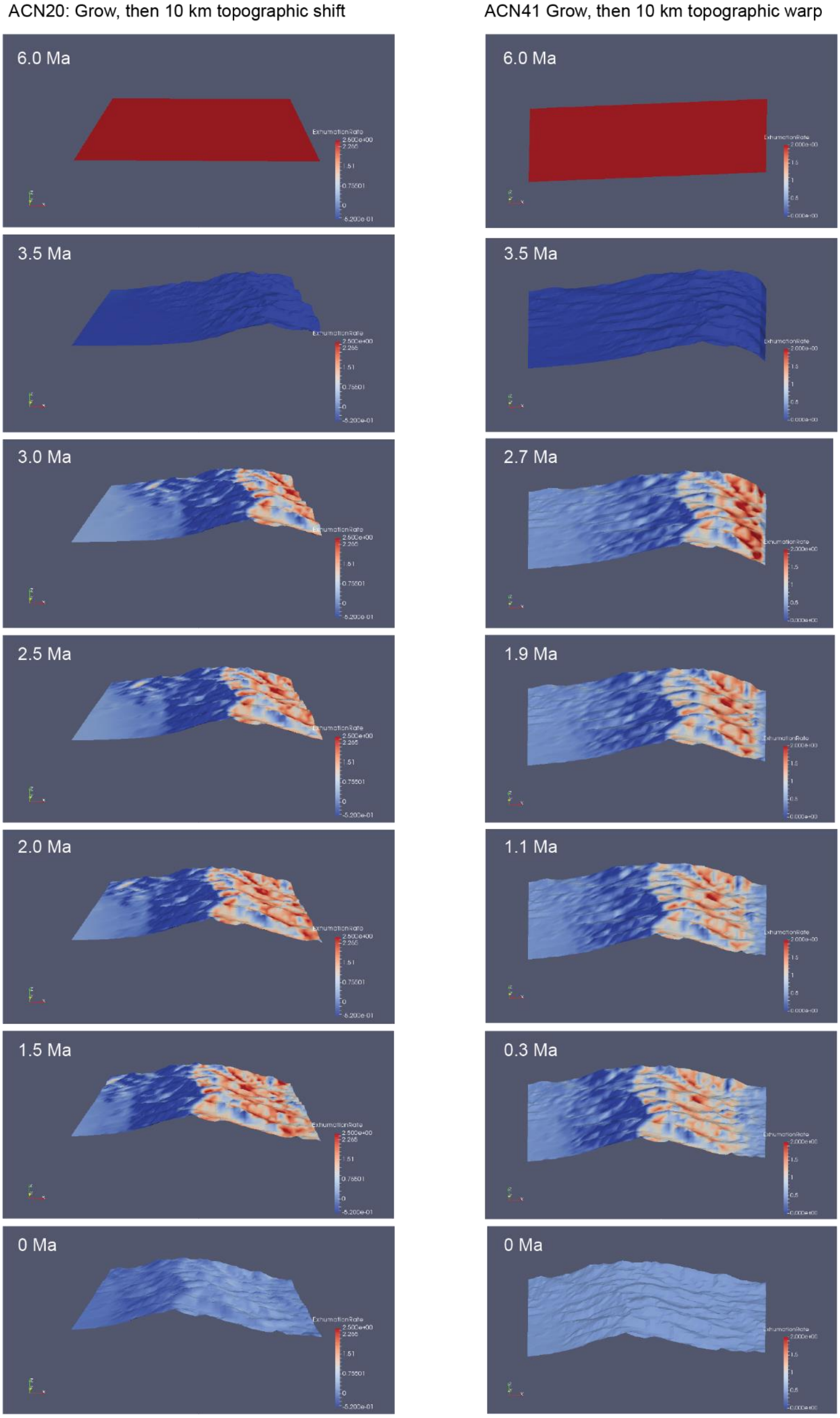

Figure S1. Snapshots of three-dimensional renditions of model simulations ACN20 (grow topography followed by 10 km of topographic shift at 4 km/My) and ACN41 (grow topography followed by 10 km of topographic warp at 2.5 km/My). Colors on surface indicate exhumation rate.

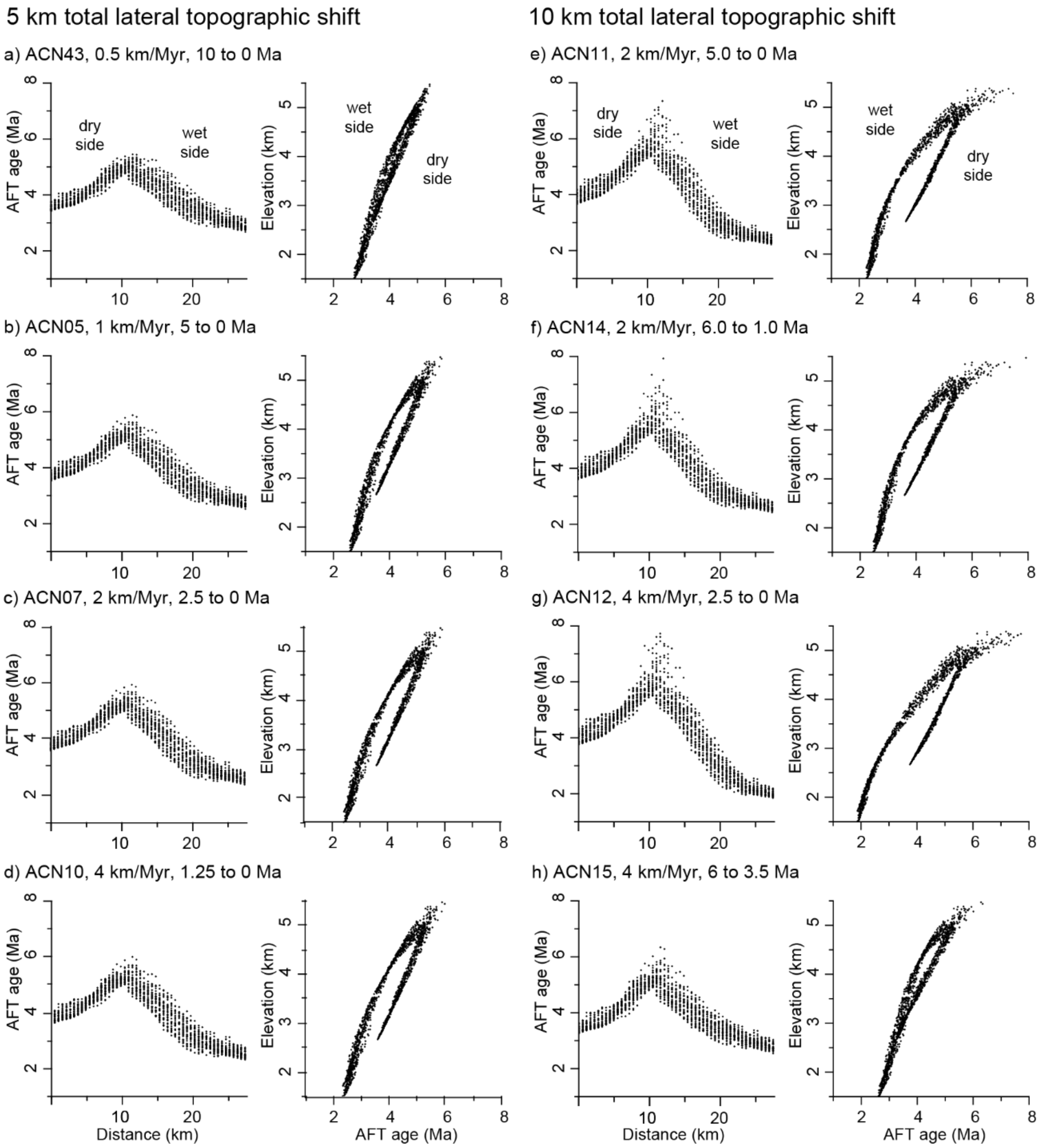

Figure S2. Predicted AFT ages plotted against latitude and elevation throughout model domain after laterally shifting topography 5 km (a-d) or 10 km (e-h). In all models, the starting and ending topography is identical to the modern topography; the lateral shift imposes a change in latitude only. A uniform background exhumation rate of 1 mm/yr is imposed starting at 6 Ma for all simulations except for a, in which it is imposed starting at 10 Ma. The time interval of shifting is indicated above each set of sub-plots. Plots a-d illustrate the effect of increasing the lateral shifting rate for a total shift of 5 km. Plots e-g show the effect of both the rate of shifting (compare e and h) and the timing of the shifting (compare e with f and g with h). The effects of differing total magnitudes of shifting are shown by comparing c with e and d with g.

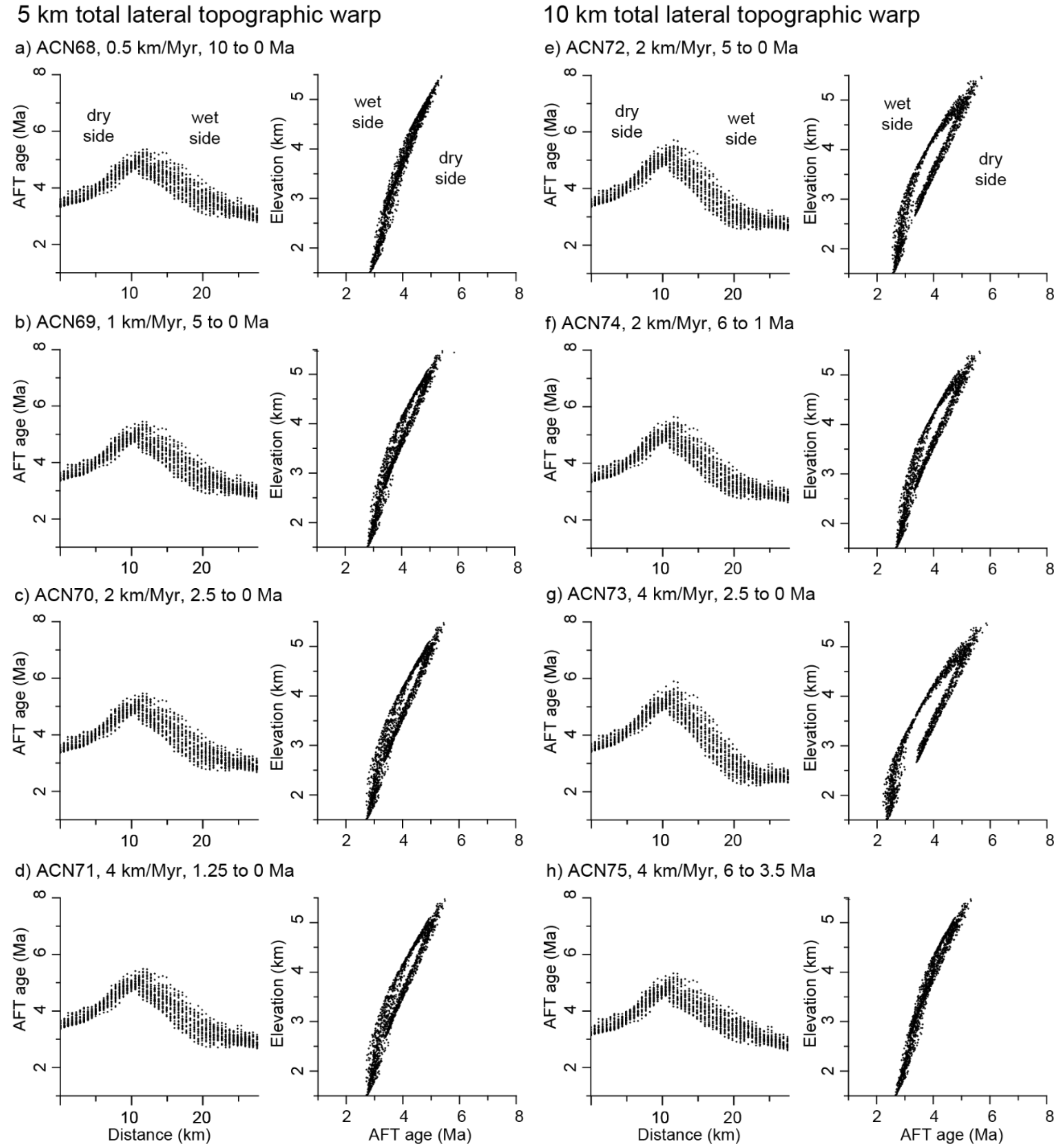

Figure S3. Predicted AFT ages plotted against latitude and elevation throughout model domain after topographic warping of 5 km (a-d) or 10 km (e-h). In all models, ending topography is identical to the modern topography; the starting topography is warped using a sine function (see main text). A uniform background exhumation rate of 1 mm/yr is imposed starting at 6 Ma for all simulations except for a, in which it is imposed starting at 10 Ma. The time interval of topographic warping is indicated above each set of sub-plots. Plots a-d illustrate the effect of increasing the warping rate for a total drainage-divide migration of 5 km. Plots e-g show the effect of both the rate of warping (compare e and h) and the timing of warping (compare e with f and g with h). The effects of differing total magnitudes of warping are shown by comparing c with e and d with g.

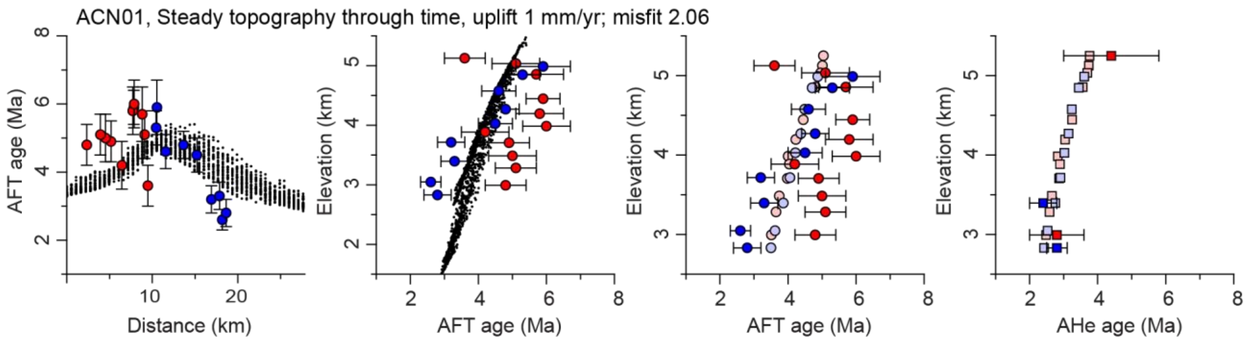

Figure S4. Comparison of reported AFT and AHe ages with model-predicted ages from Pecube simulation with steady topography and a uniform exhumation rate of 1 mm/yr. Red and blue points in each plot show reported AFT or AHe ages. Black points show model-predicted AFT ages throughout the model domain. Light blue and light red points show model-predicted AFT or AHe ages at the same location as the reported ages. Uncertainties shown for reported ages are +/- 1σ.

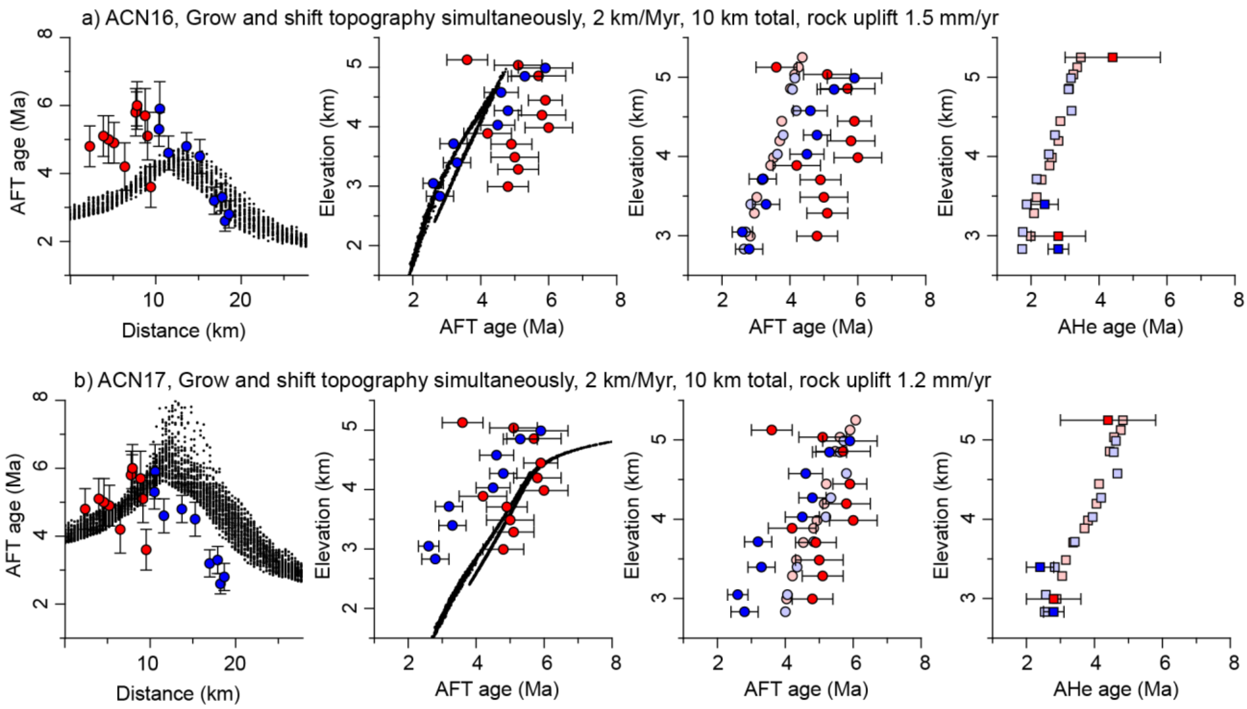

Figure S5. Comparison of reported AFT and AHe ages with model-predicted ages from Pecube simulations with topography that grows and shifts laterally simultaneously. a) Topographic shift at a rate of 2 km/Myr for a total of 10 km, with an imposed uniform exhumation rate of 1.5 mm/yr. b) Same model parameters as in (a), but with an imposed uniform exhumation rate of 1.2 mm/yr. Red and blue points in each plot show reported AFT or AHe ages. Black points show model-predicted AFT ages throughout model domain. Light blue and light red points show AFT or AHe model-predicted ages at the same location as the reported data. Uncertainties shown for reported ages are +/- 1σ.

Table S1. Thermochronology data used to constrain the thermo-kinematic models

Sample	**Longitude (ºW)**	**Latitude (ºS)**	**Elevation (m a.s.l.)**	**AFT age ±1σ (Ma)**	**# grains**	**AHe age ±1σ (Ma)**	**# grains**	**ZHe age ±1σ (Ma)**	**# grains**
ACON12	66.108350	27.201733	5250	3.6±0.6	22				
ACON11	66.108530	27.201730	5005			4.4±1.4	3/3		
ACON10	66.113350	27.193917	5035	5.1±0.7	22				
ACON9	66.113250	27.189867	4856	5.7±0.8	20				
ACON7	66.118117	27.181783	4446	5.9±0.5	20				
ACON6	66.115267	27.177250	4196	5.8±0.7	20				
ACON5	66.109300	27.172917	3984	6.0±0.7	20				
ACON4	66.120517	27.165450	3886	4.2±0.7	25				
ACON3	66.129333	27.157583	3706	4.9±0.6	20				
ACON2	66.130800	27.150400	3486	5.0±0.7	20				
ACON1	66.132833	27.144500	3283	5.1±0.6	22				
ACB1	66.158333	27.150000	2994	4.8±0.6	26	2.8±0.8	2/3	18.6±6.3	4/4
ACON20	66.041917	27.137083	4988	5.9±0.8	20				
ACON21	66.038650	27.132333	4847	5.3±0.5	20				
ACON22	66.027833	27.135983	4576	4.6±0.5	20				
ACON23	66.013950	27.149850	4270	4.8±0.4	20				
ACON24	66.005533	27.162033	4028	4.5±0.5	20				
ACON25	65.993150	27.171850	3715	3.2±0.4	20				
ACON26	65.982750	27.173533	3395	3.3±0.4	20	2.4±0.4	2/4		
ACON27	65.976516	27.171250	3047	2.6±0.3	20				
ACON28	65.973383	27.173567	2830	2.8±0.4	20	2.8±0.3	1/2	7.9±2.5	3/3

AFT: apatite fission-track; AHe: apatite (U-Th)/He; ZHe: zircon (U-Th)/He. AFT data for samples ACB1 and ACON1-ACON12 are from Sobel and Strecker (2003); AFT data for samples ACON20-ACON28 and all AHe and ZHe data are from Löbens et al (2013). Number (#) of grains reported for AFT is total number of grains counted; for AHe and ZHe: number of grains taken into account for calculating average age / total number of replicates. Uncertainty on AHe/ZHe ages is standard deviation of individual grain ages or uncertainty on single-grain age in case of single replicate.

Table S2. Thermal and age-prediction model parameters used in *Pecube*.

Parameter	**Value/reference**
Model thickness	30 / 50 km*
Model basal temperature	600 / 1000 °C*
Heat production	0.2 °C /My
Thermal diffusivity	25 km^2/My
Surface temperature at sea-level	25 °C
Atmospheric lapse rate	5 °C /km
Default age for non-reset samples	50 Ma
AFT annealing kinetics	Ketcham et al. (1999); fanning curvilinear model
AHe diffusion kinetics	Farley (2000); 100 μm grain
ZHe diffusion kinetics	Reiners et al. (2004); 100 μm grain

*Model thickness was 30 km for all models with topographic evolution only; 50 km for models including structural evolution to accommodate deep west-vergent fault – basal temperature was adjusted to maintain the same stable geothermal gradient.

References for Supplementary Material

Charreau, J., Blard, P.-H., Zumaque, J., Martin, L.C.P., Delobel, T., Szafran, L., 2019. Basinga: A cell-by-cell GIS toolbox for computing basin average scaling factors, cosmogenic production rates and denudation rates. *Earth Surf. Proc. Landf.*, 44(12), 2349-2365. https://doi.org/10.1002/esp.4649

DiBiase, R., 2018. Short communication: Increasing vertical attenuation length of cosmogenic nuclide production on steep slopes negates topographic shielding corrections for catchment erosion rates. *Earth Surf. Dyn.*, 6, 923–931. https://doi.org/10.5194/esurf-6-923-2018

Farley, K.A., 2000. Helium diffusion from apatite: General behavior as illustrated by Durango fluorapatite. *J. Geophys. Res.* 105, 2903–2914. https://doi.org/10.1029/1999jb900348

Ketcham, R.A., Donelick, R.A., Carlson, W.D., 1999. Variability of apatite fission-track annealing kinetics: III. Extrapolation to geological time scales. *American Mineralogist* 84, 1235–1255.

Martin, L.C.P., Blard, P.H., Balco, G., Lavé, J., Delunel, R., Lifton, N., Laurent, V., 2017. The CREp program and the ICE-D production rate calibration database: a fully parameterizable and updated online tool to compute cosmic-ray exposure ages. *Quat. Geochronol.* 38, 25-49. https://doi.org/10.1016/j.quageo.2016.11.006

Nishiizumi, K., Kohl, C.P., Winterer, E.L., Klein, J., Middleton, R., 1989. Cosmic ray production rates of ^{10}Be and ^{26}Al in quartz from glacially polished rocks. *J. Geophys. Res.* 94, 907–917. doi:10.1029/JB094iB12p17907

Reiners, P.W., Spell, T.L., Nicolescu, S., Zanetti, K.A., 2004. Zircon (U-Th)/He thermochronometry: He diffusion and comparisons with ^{40}Ar/^{39}Ar dating. *Geochimica et Cosmochimica Acta* 68, 1857–1887. https://doi.org/10.1016/j.gca.2003.10.021

von Blanckenburg, F., Hewawasam, T., Kubik, P.W., 2004. Cosmogenic nuclide evidence for low weathering and denudation in the wet, tropical highlands of Sri Lanka. *J. Geophys. Res.* 109, F03008. doi:10.1029/2003JF000049

Wittmann, H., Malusà, M.G., Resentini, A., Garzanti, E., Niedermann, S., 2016. The cosmogenic record of mountain erosion transmitted across a foreland basin: source-to-sink analysis of in situ ^{10}Be, ^{26}Al and ^{21}Ne in sediment of the Po river catchment. *Earth Planet. Sci. Lett*. 452, 258–271. doi:10.1016/j.epsl.2016.07.017